Microscopic theory of thermalization in one dimension with nonlinear bath coupling

A. Rodin [1,2,3,*] B. A. Olsen [1,†] M. Choi,[1] and A. Tan[1]

[1]*Yale-NUS College, 16 College Avenue West, 138527, Singapore*
[2]*Centre for Advanced 2D Materials, National University of Singapore, 117546, Singapore*
[3]*Materials Science and Engineering, National University of Singapore, 117575, Singapore*

Using a nonperturbative classical model, we numerically investigate the dynamics of mobile particles interacting with an infinite chain of harmonic oscillators, an abstraction of ionic conduction through solid-state materials. We show that coupling between the mobile particles and a single mass of the chain is sufficient to induce dissipation of the mobile particles' energy over a wide range of system parameters. When we introduce thermal fluctuations in the position of the chain mass, the mobile particles exhibit thermalization, eventually reaching the same temperature scale as the chain. This model demonstrates how a minimal set of ingredients can exhibit a link between microscopic motion and macroscopic observables, with computationally efficient simulations. Finally, we suggest some experimental platforms that could realize such a model.

I. INTRODUCTION

The relationship between microscopic particle motion and macroscopic system parameters lies at the heart of statistical mechanics, and has many implications both in basic science and technology. The fluctuation-dissipation theorem (FDT), formally established by Callen and Welton [1], demonstrated the link between viscous drag and thermal fluctuations experienced by a Brownian particle, first exposed by Einstein [2] and Smoluchowski [3]. In short, collisions between a Brownian particle and the medium hosting it drain the particle's energy, giving rise to drag and dissipation while also imparting energy to the particle due to the thermal motion of the medium.

In Brown's original experiments [4,5], the observed particles were pollen organelles colliding with water molecules. Because each Brownian particle is much heavier than the water molecules, the timescale for its motion is much longer. Therefore, the force exhibited on the particle by the water can be treated as uncorrelated white noise, an approximation which is expected to break down when the masses of the medium's constituent particles and the Brownian particle are similar. An example of such a situation is ionic motion through solid materials, where the mobile ions have similar masses to the ions constituting the lattice. Furthermore, the motion of the lattice ions is correlated due to long-range order.

Ionic transport in solids is garnering growing attention due to interest in developing solid-state batteries [6–8]. One of this technology's integral components is the solid-state electrolyte: an electronically insulating material that can conduct ions and serves as a separator between the anode and the cathode. One recent approach proposed a microscopic theory to describe the dissipative motion of ions through crystalline solids [9]. In the limit of high temperature and long time, the effect of correlations is severely diminished, and FDT can relate random thermal forces to drag in the material.

The problem of a small mobile particle coupled to a dissipative thermal bath has been of interest to the physics community for a long time [10,11]. In recent years, there have been significant advances in understanding the dynamics of impurities immersed in bosonic [12–16] and fermionic [12,17,18] systems. In recent work, linearized approaches have been used to show the emergence of Brownian motion in D-dimensional Bose-Einstein condensates [19], as well as the microscopic origins of friction in one-dimensional quantum liquids [20]. Some related approaches to studying classical thermalization in microscopic systems are based on the Fermi-Pasta-Ulam-Tsingou problem [21,22].

In this work, we build on the formalism from Ref. [9] to approach ion transport from a classical perspective. We construct a minimal experimentally realizable model to show how particles trapped in a harmonic potential and coupled to an "ion framework" composed of a one-dimensional chain of harmonic oscillators can exhibit both dissipation and thermalization. We demonstrate that interactions between the mobile particles and a single mass of the chain are sufficient to induce fluctuation-dissipation behavior. One advantage of our classical approach is that it does not rely on the assumption that the displacement of the chain masses is small. In contrast, most quantum-mechanical formulations of the interaction between mobile particles and oscillator baths use a coupling that is linear in the oscillator coordinate [14,16,17,19].

In Sec. II, we derive the integrodifferential equations of motion for a collection of mobile particles traveling through a potential landscape generated by a vibrating lattice of

---

*Corresponding author: aleksandr.rodin@yale-nus.edu.sg
†Corresponding author: ben.olsen@yale-nus.edu.sg

arbitrary dimensionality. In Sec. III, we simplify those equations for a one-dimensional system with a specific lattice geometry, and describe the computational procedure for numerically simulating the particle trajectories. To disentangle the effects of dissipation and fluctuation, in Sec. IV we explore the behavior of systems at $T = 0$. We test the scaling of dissipation with system parameters, and discuss the role of the "memory" term arising from integrating out the chain degrees of freedom. In Sec. V, we study the role of fluctuations on particle trajectories by varying the temperature of the lattice. Finally, we propose some potential platforms for experimental validation of this model using cold atoms or ions in Sec. VI.

II. GENERAL MODEL

We begin by considering a general Lagrangian (in spatial dimension D) describing the motion of mobile particles through a framework of masses with vibrational modes,

$$L = T_M(\dot{\mathbf{R}}) - V_M(\mathbf{R}) + T_F(\dot{\mathbf{r}}) - V_F(\mathbf{r}) - U(\mathbf{r}, \mathbf{R}, t). \quad (1)$$

Here we combine the displacements of the framework masses from their equilibrium positions into a single vector $\mathbf{r} = \bigoplus_{j=1} \mathbf{r}_j$, and combine the mobile particle positions as $\mathbf{R}$. $T_M(\dot{\mathbf{R}})$ and $T_F(\dot{\mathbf{r}})$ are the kinetic energies of the mobile particles and framework masses, respectively, while $V_M(\mathbf{R})$ and $V_F(\mathbf{r})$ are the corresponding time-independent potential energies. Finally, $U(\mathbf{r}, \mathbf{R}, t)$ is a general potential energy that describes all remaining interactions and perturbations.

Assuming the homogeneous motion of the framework masses is harmonic, we write

$$T_F(\mathbf{r}) - V_F(\mathbf{r}) \rightarrow \frac{1}{2}\dot{\mathbf{r}}^T \overleftrightarrow{m} \dot{\mathbf{r}} - \frac{1}{2}\mathbf{r}^T \overleftrightarrow{V} \mathbf{r}. \quad (2)$$

Here, $\overleftrightarrow{m} = \bigoplus_{j=1} m_j \overleftrightarrow{1}_D$ is a block-diagonal matrix where m_j is the mass of the jth framework mass, and $\overleftrightarrow{V}$ is the harmonic coupling matrix.

The homogeneous equation of motion $\overleftrightarrow{m}\ddot{\mathbf{r}} = -\overleftrightarrow{V}\mathbf{r}$ obtained from Eq. (2) can be transformed into a symmetric eigenvalue problem by first defining $\tilde{\mathbf{r}} = \overleftrightarrow{m}^{\frac{1}{2}}\mathbf{r}$ so that

$$\ddot{\tilde{\mathbf{r}}} = -\Omega_j^2 \tilde{\mathbf{r}} = -\overleftrightarrow{m}^{-\frac{1}{2}}\overleftrightarrow{V}\overleftrightarrow{m}^{-\frac{1}{2}}\tilde{\mathbf{r}} \equiv -\overleftrightarrow{\tilde{V}}\tilde{\mathbf{r}}, \quad (3)$$

with normalized eigenvectors $\boldsymbol{\varepsilon}_j$ and corresponding eigenvalues Ω_j^2. Hence, we can write $\tilde{\mathbf{r}}(t) = \overleftrightarrow{\varepsilon}\boldsymbol{\zeta}(t)$ and, consequently, $\mathbf{r}(t) = \overleftrightarrow{m}^{-\frac{1}{2}}\overleftrightarrow{\varepsilon}\boldsymbol{\zeta}(t)$, where $\boldsymbol{\zeta}(t)$ is a column vector of normal coordinates giving the amplitude of each mode, and $\overleftrightarrow{\varepsilon} = [\boldsymbol{\varepsilon}_1, \boldsymbol{\varepsilon}_2, \dots]$ is a row of column vectors $\boldsymbol{\varepsilon}_j$.

Writing the equations of motion for the framework masses using all the terms in Eq. (1) yields

$$\overleftrightarrow{m}\ddot{\mathbf{r}} = -\overleftrightarrow{V}\mathbf{r} - \nabla_{\mathbf{r}}U(\mathbf{r}, \mathbf{R}, t),$$
$$\rightarrow \ddot{\boldsymbol{\zeta}} = -\overleftrightarrow{\Omega}^2\boldsymbol{\zeta} - \overleftrightarrow{\varepsilon}^{-1}\overleftrightarrow{m}^{-\frac{1}{2}}\nabla_{\mathbf{r}}U(\mathbf{r}, \mathbf{R}, t), \quad (4)$$

where $\overleftrightarrow{\Omega}^2 = \overleftrightarrow{\varepsilon}^{-1}\overleftrightarrow{\tilde{V}}\overleftrightarrow{\varepsilon}$ is a diagonal matrix of the squared eigenfrequencies. For a single normal coordinate, the equation of motion takes the form $\ddot{\zeta}_j = -\Omega_j^2\zeta_j - f_j$, which can be solved using the Green's function formalism. Recalling that

the Green's function for a harmonic oscillator is given by

$$G_j(t, t') = \frac{\sin[\Omega_j(t - t')]}{\Omega_j}\Theta(t - t'), \quad (5)$$

we have

$$\zeta_j(t) = \zeta_j^H(t) - \int^t dt' \frac{\sin[\Omega_j(t - t')]}{\Omega_j}$$
$$\times [\overleftrightarrow{\varepsilon}^{-1}\overleftrightarrow{m}^{-\frac{1}{2}}\nabla_{\mathbf{r}}U(\mathbf{r}, \mathbf{R}, t')]_j$$
$$= \zeta_j^H(t) - \int^t dt' \frac{\sin[\Omega_j(t - t')]}{\Omega_j}$$
$$\times \boldsymbol{\varepsilon}_j^T\overleftrightarrow{m}^{-\frac{1}{2}}\nabla_{\mathbf{r}}U(\mathbf{r}, \mathbf{R}, t'), \quad (6)$$

where $\zeta_j^H(t)$ is the homogeneous solution and the subscript j at the braces indicates that we pick out the jth element of the column vector. The second equality follows from the fact that $\overleftrightarrow{\varepsilon}$ is an orthogonal matrix so that $\overleftrightarrow{\varepsilon}^{-1} = \overleftrightarrow{\varepsilon}^T$. Using $\mathbf{r}(t) = \overleftrightarrow{m}^{-\frac{1}{2}}\sum_j \boldsymbol{\varepsilon}_j\zeta_j(t)$, we obtain

$$\mathbf{r}(t) = \overleftrightarrow{m}^{-\frac{1}{2}}\sum_j \boldsymbol{\varepsilon}_j\zeta_j^H(t)$$
$$- \int^t dt'\overleftrightarrow{m}^{-\frac{1}{2}}\overleftrightarrow{G}(t - t')\overleftrightarrow{m}^{-\frac{1}{2}}\nabla_{\mathbf{r}}U(\mathbf{r}, \mathbf{R}, t'), \quad (7)$$
$$\overleftrightarrow{G}(\tau) = \sum_j \boldsymbol{\varepsilon}_j \otimes \boldsymbol{\varepsilon}_j \frac{\sin(\Omega_j\tau)}{\Omega_j}. \quad (8)$$

The homogeneous solution $\zeta_j^H(t)$ is determined by the thermodynamic properties of the framework. To relate the amplitudes of the modes to the framework temperature, we consider the Lagrangian for a single normal mode ζ_j, given by $L_j = \dot{\zeta}_j^2/2 - \Omega^2\zeta_j^2/2$. The solution to the resulting equation of motion is $\zeta_j(t) = A_j\cos(\Omega_j t + \phi_j)$, where $0 \leqslant \phi_j < 2\pi$ is a phase factor determined by boundary conditions.

To generate the $\mathbf{r}(t)$ originating from the thermal motion, we obtain a set of ϕ_j and A_j that correctly reflect the system's thermodynamics. The phases ϕ_j are sampled from a uniform distribution $[0, 2\pi)$. To generate the amplitudes A_j, we recall that the amplitude is related to the total energy of the oscillator mode, which is temperature dependent. If we used the Boltzmann distribution to generate the amplitudes, at low enough temperatures, there would be no motion in the chain. Therefore, we treat the possible energies of each mode as a discrete spectrum, following the solution of the quantum-mechanical harmonic oscillator. Then the amplitudes become functions of the number of quanta n: $A_j(n)$. The resulting expectation value of the square of the displacement is

$$\langle\zeta_j(t)\zeta_j(t)\rangle = \oint \frac{d\phi_j}{2\pi}\frac{\sum_n A_j^2(n)\cos^2(\Omega_j t + \phi_j)e^{-n\Omega_j/\Omega_T}}{\sum_n e^{-n\Omega_j/\Omega_T}}$$
$$= \frac{1}{2}\frac{\sum_n A_j^2(n)e^{-n\Omega_j/\Omega_T}}{\sum_n e^{-n\Omega_j/\Omega_T}}, \quad (9)$$

where $\Omega_T = k_B T/\hbar$ is the thermal frequency. Recalling the familiar result for a quantum harmonic oscillator $\langle\zeta_j(t)\zeta_j(t)\rangle = \frac{\hbar}{\Omega_j}[n_B(\Omega_j) + \frac{1}{2}]$, where n_B is the Bose-Einstein distribution,
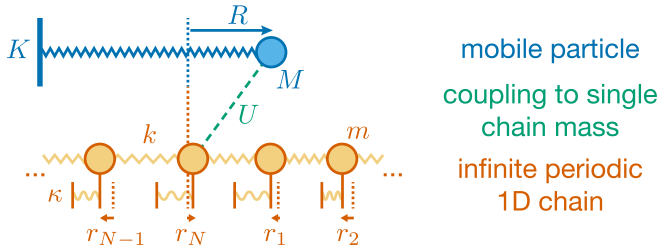
FIG. 1. *Schematic of the system.* A mobile particle of mass M undergoes 1D harmonic motion with spring constant K and displacement from equilibrium R. It couples via potential U to the Nth mass from a periodic 1D chain of $N \rightarrow \infty$ masses, each of which undergoes harmonic motion with spring constant κ and displacement r_g and couples to its neighbor with spring constant k. The 1D chain has N modes of finite bandwidth and acts as a bath, so the coupling leads to fluctuation and dissipation of the mobile mass's motion.

we find that $A_j(n_j) = \sqrt{n_j + \frac{1}{2}}\sqrt{\frac{2\hbar}{\Omega_j}}$, where n_j is an integer obtained from the probability distribution $e^{-n\Omega_j/\Omega_T}$.

The second term in Eq. (7) encapsulates all of the interactions in the system. Since this term integrates a generalized force for all past times, we refer to it as the "memory" term in the trajectory, and $\overleftrightarrow{G}$ as the "memory kernel." While formally the memory is integrated over all past times, we will explore the consequences of truncating the integration in Sec. IV C.

The advantage of the memory formalism becomes evident when writing the the equations of motion for the mobile particles

$$\overleftrightarrow{M}\ddot{\mathbf{R}} = -\nabla_{\mathbf{R}}[U(\mathbf{r}, \mathbf{R}, t') + V_M(\mathbf{R})], \qquad (10)$$

where $\overleftrightarrow{M} = \bigoplus_j M_j \overleftrightarrow{1}_D$ is the equivalent of $\overleftrightarrow{m}$ for the mobile particles. In order to obtain the trajectories of the mobile particles, we see that we can neglect the components of $\mathbf{r}$ which do not appear in $U(\mathbf{r}, \mathbf{R}, t)$. With this restriction, Eq. (7) allows us to solve only the relevant components of $\mathbf{r}$ and ignore other degrees of freedom. This simplification becomes more dramatic if the mobile particles interact with a small fraction of the framework masses. In this way, if the number of extraneous degrees of freedom of the framework is large enough, it can act as a thermal bath able to exchange energy with the mobile particles via the interaction U.

III. ONE-DIMENSIONAL CHAIN

A. Problem formulation

The simplest system with sufficient extraneous degrees of freedom to act as a heat bath is shown in Fig. 1. In this setup, the framework is composed of a periodic chain of $N \rightarrow \infty$ identical masses m connected by identical springs with force constant k and restricted to one-dimensional (1D) motion. Each chain mass is also confined by an external harmonic potential with force constant κ to suppress zero-frequency modes which can cause instabilities in low-dimensional systems. The vibrational eigenmodes have frequencies

$$\Omega_j = \sqrt{\frac{\kappa}{m} + 4\frac{k}{m}\sin^2\left(\frac{\pi j}{N}\right)}$$

$$= \sqrt{\Omega_{\min}^2 \cos^2\left(\frac{\pi j}{N}\right) + \Omega_{\max}^2 \sin^2\left(\frac{\pi j}{N}\right)} \qquad (11)$$

with corresponding normalized eigenvectors $\varepsilon_{g,j}^{\cos} = \cos(q_j g)\sqrt{2/N}$ and $\varepsilon_{g,j}^{\sin} = \sin(q_j g)\sqrt{2/N}$ for $q_j = 2\pi j/N$ with $1 \leqslant j \leqslant N/2$, where $1 \leqslant g \leqslant N$ is the index of the chain particle. Here, $\Omega_{\max} = \sqrt{4k/m + \kappa/m}$ and $\Omega_{\min} = \sqrt{\kappa/m}$ are the maximum and minimum frequencies of the eigenmodes, which form an acoustic phonon band.

The mobile particles, each of mass M, move in 1D parallel to the chain and experience a harmonic potential with force constant K. The minimum of this potential coincides with the minimum of the harmonic well containing the Nth chain particle, as shown in Fig. 1. The mobile particles do not interact with each other, so $V_M = \frac{1}{2}K\sum_j R_j^2$ in Eq. (10). In addition, the interactions are restricted to pairwise couplings between the chain mass and the mobile particles and do not contain an explicit time dependence, allowing us to write $U(\mathbf{r}, \mathbf{R}, t)$ as $U(r_N, \mathbf{R}) = \sum_j U(r_N, R_j)$.

Because only the Nth chain particle interacts with the mobile particles, it is the only mass whose position is relevant to the system dynamics. Consequently, $\mathbf{r}$ in Eq. (7) contains a single entry r_N. Moreover, we retain only the Nth element of the eigenvectors $\varepsilon_{N,j}^{\cos} = \sqrt{2/N}$, $\varepsilon_{N,j}^{\sin} = 0$, resulting in

$$r_N(t) = \sqrt{\frac{2}{N}}\frac{1}{\sqrt{m}}\sum_j \sqrt{n_j + \frac{1}{2}}\sqrt{\frac{2\hbar}{\Omega_j}}\cos(\Omega_j t + \phi_j)$$
$$- \frac{1}{m}\int^t dt' G(t - t')\frac{dU[r_N(t'), \mathbf{R}(t')]}{dr_N}, \qquad (12)$$

$$G(t) = \frac{2}{N}\sum_{j=1}^{N/2}\frac{\sin(\Omega_j t)}{\Omega_j}$$
$$= \frac{2}{\pi}\int_{\Omega_{\min}}^{\Omega_{\max}} dz \frac{\sin(tz)}{\sqrt{z^2 - \Omega_{\min}^2}\sqrt{\Omega_{\max}^2 - z^2}}, \qquad (13)$$

$$\ddot{R}_j(t) = \frac{1}{M}\left\{-\frac{d}{dR_j}U[r_N(t), R_j(t)] - KR_j(t)\right\}. \qquad (14)$$

Since we are interested primarily in the motion of the mobile particles, we define several characteristic scales: $\Omega_M = \sqrt{K/M}$ is the homogeneous oscillation frequency of the mobile particles, with period $t_M = 2\pi/\Omega_M$ and energy $E_M = \hbar\Omega_M = Kl_M^2$, where $l_M = \sqrt{\hbar/M\Omega_M}$ is the quantum oscillator length. Rewriting Eqs. (12)–(14) in terms of these characteristic quantities and expressing m as a multiple of M yields

$$\rho(\tau) = \sqrt{\frac{2}{N}}\sum_j \sqrt{n_j + \frac{1}{2}}\sqrt{\frac{2}{\mu\omega_j}}\cos(2\pi\omega_j\tau + \phi_j)$$
$$- \frac{2\pi}{\mu}\int^\tau d\tau'\Gamma(\tau - \tau')\sum_j \frac{d\Phi[\rho(\tau'), \sigma_j(\tau')]}{d\rho}, \qquad (15)$$

$$\Gamma(\tau) = \frac{2}{\pi}\int_{\omega_{\min}}^{\omega_{\max}} dx \frac{\sin(2\pi\tau x)}{\sqrt{x^2 - \omega_{\min}^2}\sqrt{\omega_{\max}^2 - x^2}}, \qquad (16)$$

$$\ddot{\sigma}_j(\tau) = (2\pi)^2\left\{-\frac{d}{d\sigma_j}\Phi[\rho(\tau), \sigma_j(\tau)] - \sigma_j(\tau)\right\}. \qquad (17)$$

TABLE I. *Parameters used in the model.* In the simulations, we formulate the dynamics using dimensionless quantities, given in the right column. This formulation leads to values for most quantities on the order of unity, which helps avoid numerical issues due to machine precision. Here, $\Omega_M = \sqrt{K/M}$, $t_M = 2\pi/\Omega_M$, $E_M = \hbar\Omega_M = Kl_M^2$, and $l_M = \sqrt{\hbar/M\Omega_M}$.

Parameter		Dimensionless
Chain mass position	r	$\rho = r/l_M$
Mobile mass position	R	$\sigma = R/l_M$
Evolution time	t	$\tau = t/t_M$
Chain particle mass	m	$\mu = m/M$
Frequency	Ω	$\omega = \Omega/\Omega_M$
Interaction strength	U	$\Phi = U/E_M$
Memory kernel	G	$\Gamma = G \cdot \Omega_M$
Interaction length	s	$\lambda = s/l_M$
Mobile particle energy	E	$\mathcal{E} = E/E_M$
Thermal frequency	Ω_T	$\omega_T = k_B T/E_M$

Note that we dropped the subscript N because it is redundant as we are keeping track of a single chain mass. To help keep track of the correspondence between regular and dimensionless parameters of the model, we collect them in Table I.

The harmonic potential of the mobile particle allows multiple interactions with the chain mass, mimicking transport in a crystal, where it would interact with many different masses in the chain. Therefore, Ω_M is chosen to be smaller than other energy scales so that the kinetic energy of the mobile particle does not change due to the potential during its interaction with the chain.

Despite the simplifications due to the 1D geometry, Eqs. (15)–(17) are still not tractable analytically and require a numerical approach to compute the trajectories.

B. Computational procedure

Numerically integrating Eqs. (15) and (17), while conceptually straightforward, can be computationally demanding. We performed our computations using the JULIA programming language [23], and our code is available in [24]. JULIA is well suited for scientific computing due to a number of native optimizations. All our plots are visualized using MAKIE.JL [25] and employ a scheme suitable for color-blind readers, developed in [26].

Here we describe the computational techniques that complement the scripts in [24] to reproduce all the calculations presented in the following sections. We do not provide the output files because of their size, but we do include the scripts used to generate them.

By rewriting Eqs. (15) and (17) using discrete time steps δ so that $\tau = \delta\alpha$ for integer α's, we have

$$\rho_\alpha = \sqrt{\frac{2}{N}} \sum_j \sqrt{n_j + \frac{1}{2}} \sqrt{\frac{2}{\mu\omega_j}} \cos(2\pi\omega_j\delta\alpha + \phi_j)$$

$$- \frac{2\pi\delta}{\mu} \sum_\beta \Gamma[\delta(\alpha - \beta)] \sum_j \frac{d\Phi(\rho_\beta, \sigma_{j,\beta})}{d\rho},$$

$$\sigma_{j,\alpha} = (2\pi\delta)^2 \left[-\frac{d}{d\sigma_j} \Phi(\rho_{\alpha-1}, \sigma_{j,\alpha-1}) - \sigma_{j,\alpha-1} \right]$$
$$+ 2\sigma_{j,\alpha-1} - \sigma_{j,\alpha-2}. \tag{18}$$

These difference equations can be solved using iteration, as is common for initial value problems. In our case, we initialize $\sigma_{j,0}$ and $\sigma_{j,1}$ to the same value to have the mobile particles start from rest.

To guarantee the smoothness of the solution, it is important to consider two factors. First, the time step δ has to be much smaller than the period of the fastest chain mode. Second, δ has to be sufficiently small so that the force experienced by the rapidly moving mobile particles is smooth in the vicinity of the chain particle with which they interact. We will illustrate the fulfillment of these conditions in the following section.

Because ρ_α and $\sigma_{j,\alpha}$ in Eq. (18) depend on the earlier positions, the solution of the difference equation is not parallelizable, which slows down the calculation. Fortunately, we can alleviate some of the computational load by precomputing the memory kernel Γ. We first define the time period for the simulation $\tau \in [0, \tau_f]$ and partition this period into steps of size δ, where δ is chosen to satisfy the requirements described above. Next, we calculate an array $[\Gamma(\delta), \Gamma(2\delta), \ldots, \Gamma(\tau_f)]$ by integrating Eq. (16) using the Gaussian quadrature method. Because the entries of the array are independent of one another, they can be computed in parallel. Precomputing the memory kernel eliminates the slow integration step from the sequential solution of Eq. (18), leaving only algebraic calculations.

In the course of the simulation, we save the force terms $\sum_j \frac{d}{d\rho}\Phi(\rho_\alpha, \sigma_{j,\alpha})$ and $\frac{d}{d\sigma_j}\Phi(\rho_{\alpha-1}, \sigma_{j,\alpha-1})$ for each time step. We can then calculate the memory term by multiplying the "past" forces by the appropriate entries of the precomputed Γ array and performing a summation. Here $\Gamma(0)$ is multiplied by the current force, $\Gamma(\delta)$ by the force from the previous step, $\Gamma(2\delta)$ by the force from two steps ago, and so on. That is, Γ's with larger time arguments get multiplied by "older" forces.

Although the exact form of the interaction between mobile particles and the chain mass will lead to some quantitative differences in the particle trajectory, we expect the qualitative behavior to be independent of the details of the potential. Therefore, for the sake of simplicity, we choose $\Phi = \Phi_0 \exp[-(\rho_\alpha - \sigma_{j,\alpha})^2/2\lambda^2]$, where $F = \hbar\Omega_M\Phi_0$ is the interaction amplitude, and $s = \lambda l_M$ is the characteristic length scale of the interaction.

The final ingredient of the simulation is the homogeneous, or thermal, motion of the chain particle. To compute the trajectory for 10^6 chain masses, we generate 5×10^5 equally spaced values q_j between 0 and π, along with the corresponding frequencies ω_j given by Eq. (11). Next, we generate 5×10^5 random phases $0 \leqslant \phi_j \leqslant 2\pi$, as well as random integers n_j from the probability distribution $e^{-n\omega_j/\omega_T}$. These values of n_j and ϕ_j are then used to construct the trajectory $\rho^H(\tau) = \sum_j \sqrt{n_j + \frac{1}{2}} \sqrt{\frac{4}{N\mu\omega_j}} \cos(2\pi\omega_j\tau + \phi_j)$, as shown in Eq. (15).
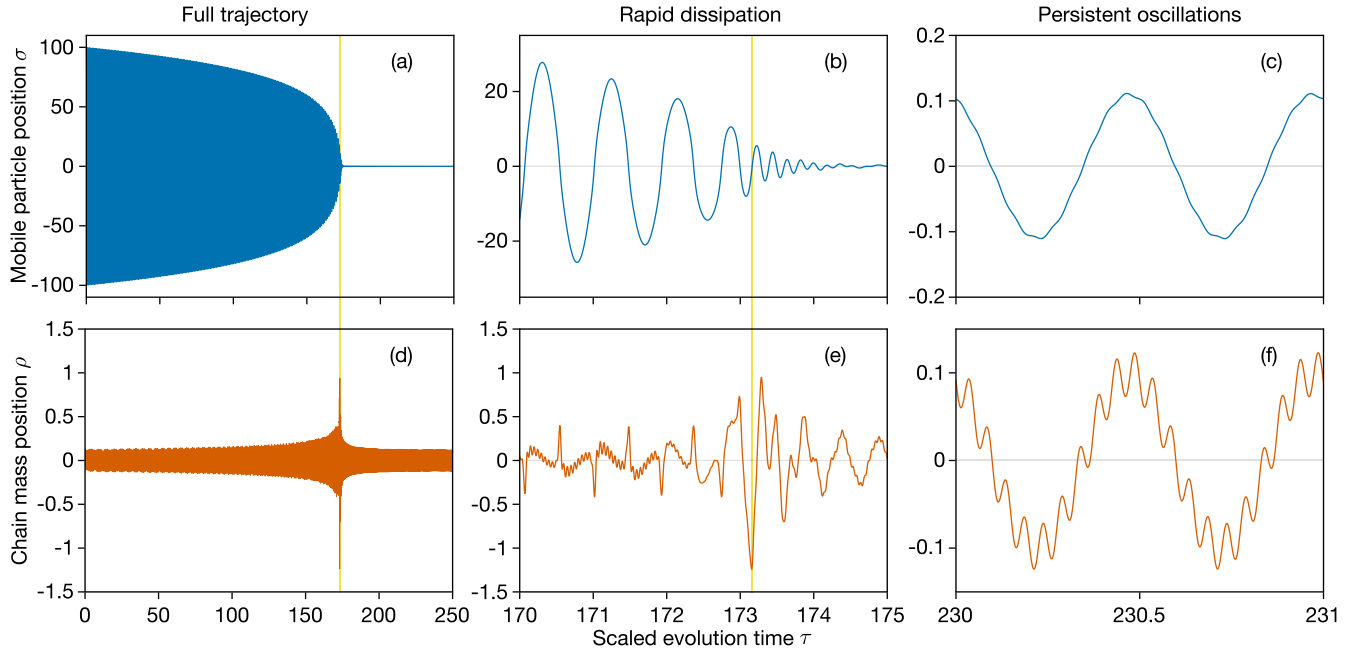
FIG. 2. *General example with a single mobile particle.* Trajectories $\sigma(\tau)$, $\rho(\tau)$ for the mobile particle and the interacting chain particle, respectively. Here we chose $\omega_{\min} = 2$, $\omega_{\max} = 20$, $\mu = 2$, $\lambda = 4$, $\Phi_0 = -500$ with $\sigma(0) = 100$ and $\rho(0) = 0$. The mobile particle undergoes many oscillations and its energy slowly dissipates until about $\tau = 172$. Dissipation then quickly reduces its energy to nearly zero, and it falls into the potential well of the interacting chain particle, which reaches its largest displacement at around $\tau = 173$, indicated by the vertical yellow line. For late times $\tau > 175$, both particles undergo small, persistent, nondissipative oscillations at two frequencies just outside the phonon band of the chain.

IV. DISSIPATION

A. General picture

To develop a better feel for the system behavior, we will begin by studying trajectories with vanishing thermal motion $\rho^H = 0$. In this case, we expect the mobile particles to dissipate energy over time due to their interaction with the chain.

As a first example, we choose a configuration with a single mobile particle and set $\omega_{\min} = 2$, $\omega_{\max} = 20$, $\mu = 2$, $\lambda = 4$, and $\Phi_0 = -500$ (attractive interaction). The trajectory for these parameters is shown in Fig. 2. We chose $\omega_{\min}$ to be small to mimic phonon dispersion in real materials, but larger than the mobile particle's harmonic trap frequency, as discussed above. Our choice of $\omega_{\max} = 20$ is a compromise between providing a wide band and keeping a reasonable computational load, as discussed below. Other values of $\omega_{\min}$ and $\omega_{\max}$ produce qualitatively similar results. We set the time step δ of the simulation to be substantially smaller than the period of the fastest chain mode $\tau_{\max} = (2\pi/\Omega_{\max})/(2\pi/\Omega_M) = 1/\omega_{\max}$. When written in terms of dimensionless quantities, periods and frequencies satisfy $\omega\tau = 1$ (while $\Omega t = 2\pi$). For our calculations, $\delta = 1/60\omega_{\max}$.

In Fig. 2, we can identify two qualitatively distinct regimes. For $\tau < 172$, the mobile particle essentially undergoes simple harmonic motion with gradually decreasing amplitude. Because the oscillation amplitude is much larger than the range of the interaction λ, the mobile particle spends very little time interacting with the chain, which explains why the oscillations are almost sinusoidal. The amplitude of the chain mass motion grows slowly. Intuitively, when the mobile

particle passes the chain mass, the latter is displaced due to the interaction term. As the amplitude of the mobile particle's motion decreases, the speed with which it passes the chain mass becomes smaller. Consequently, the time of the interaction grows, leading to an increase of the chain mass displacement.

From the trajectories in the first column of Fig. 2, the total energy of the two-particle system appears not to be conserved. However, the total energy of the closed system is distributed among the mobile particle and the $N \to \infty$ chain modes. In our calculations, we do not keep track of all the chain masses and are, therefore, unable to use the motion of the chain to compute its energy. This loss of information is a consequence of integrating out the degrees of freedom into the memory kernel, which allows us to study an infinitely long system by only focusing on its single component.

For $\tau > 175$, the motion of the two particles appears to be a superposition of two modes with the slower one being in phase for the two objects and the faster one being completely out of phase. Moreover, the amplitude of the oscillations appears to persist over many cycles, suggesting a lack of energy dissipation. To confirm that this nondissipative motion is not a numerical artifact, we explore the long-term system behavior when $|\rho - \sigma| \ll \lambda$. In this case, the Gaussian interaction term can be expanded to yield

$$\rho(\tau) = \frac{2\pi \Phi_0}{\mu \lambda^2} \int_{-\infty}^{\infty} d\tau' \Theta(\tau - \tau')$$

$$\times \frac{2}{N} \sum_{j=1}^{N/2} \frac{\sin[2\pi\omega_j(\tau - \tau')]}{\omega_j} [\rho(\tau') - \sigma(\tau')],$$

$$\ddot{\sigma}(\tau) = (2\pi)^2 \left\{ \frac{\Phi_0}{\lambda^2} [\sigma(\tau) - \rho(\tau)] - \sigma(\tau) \right\}, \qquad (19)$$

where we extended the lower time limit to $-\infty$ to focus on the long-term behavior. Taking the Fourier transform of this system of equations using the definition $g_\omega = \mathcal{F}[g(\tau)] = (2\pi)^{-1/2} \int_{-\infty}^{\infty} d\tau \, e^{i2\pi\omega\tau} g(\tau)$ gives

$$\rho_\omega = \frac{2\pi\Phi_0}{\mu\lambda^2} \frac{2}{N} \sum_{j=1}^{N/2} \left[\frac{i\pi}{2\omega_j} [\delta(\omega - \omega_j) - \delta(\omega + \omega_j)] \right.$$
$$\left. - \frac{2\pi}{4\pi^2\omega^2 - 4\pi^2\omega_j^2} \right] (\rho_\omega - \sigma_\omega),$$

$$-(2\pi\omega)^2 \sigma_\omega = (2\pi)^2 \left[\frac{\Phi_0}{\lambda^2} (\sigma_\omega - \rho_\omega) - \sigma_\omega \right]. \qquad (20)$$

We included the factor of 2π inside the exponential to agree with the argument form of the memory kernel. From the Fourier transform, we see that only if $\omega \notin [\omega_{\min}, \omega_{\max}]$, the delta functions both vanish and the system of equations may admit persistent real-ω solutions. Therefore, we drop the delta functions to get $\rho_\omega = \frac{\Phi_0}{\mu\lambda^2}(\sigma_\omega - \rho_\omega)f_\omega$ with

$$f_\omega = \frac{2}{N} \sum_{j=1}^{N/2} \frac{1}{\omega^2 - \omega_j^2} = \frac{1}{\omega^2 - \omega_{\max}^2} \sqrt{\frac{\omega^2 - \omega_{\max}^2}{\omega^2 - \omega_{\min}^2}}. \qquad (21)$$

Eliminating ρ_ω and σ_ω from the system of equations yields

$$(1 - \omega^2)\left(1 + \frac{f_\omega \Phi_0}{\mu\lambda^2}\right) = \frac{\Phi_0}{\lambda^2}. \qquad (22)$$

Solving Eq. (22) for the parameters used in the simulation reveals that there indeed are two persistent modes: one at $\omega \approx 0.999\omega_{\min}$ and another at $\omega \approx 1.001\omega_{\max}$. Because these two modes are outside the phonon band, they do not couple with the chain modes and, therefore, do not dissipate energy. This effect persists even when the $\rho^H(\tau)$ term is included, provided the random thermal noise is sufficiently weak. Raising the temperature further will disrupt this periodic motion, as we will see below.

B. Dissipation scaling

In the previous section, we discussed dissipation of a single mobile particle's energy for a particular choice of system parameters. We now address how the choice of these parameters determines the dissipation rate. To make analytical progress, we focus on the regime where the amplitude of the mobile particle's oscillations is substantially larger than the extent of the interaction potential.

To estimate the amount of energy that the mobile particle loses after a single encounter with the chain mass, we neglect the confining potential and assume that the particle travels at a constant speed from negative infinity so that $\sigma(\tau) = \dot{\sigma}_0\tau$. This simplification is reasonable if the gain in the kinetic energy due to the harmonic trap in the vicinity of the chain mass is negligible. Next, we assume that the displacement of the chain mass is sufficiently small so that it can be dropped from the

integral in Eq. (15), leading to

$$\rho(\tau) = \frac{2\pi}{\mu} \int_{-\infty}^{\tau} d\tau' \Gamma(\tau - \tau') \frac{d}{d\sigma} \Phi[\sigma(\tau')], \qquad (23)$$

where we used $d\Phi/d\rho = -d\Phi/d\sigma$.

To estimate the speed of the chain mass at $\tau = 0$ (as the mobile particle passes the origin), we differentiate Eq. (23) with respect to τ:

$$\dot{\rho}(0) = \frac{2\pi}{\mu} \int_{-\infty}^{0} d\tau' \dot{\Gamma}(-\tau') \frac{d\Phi}{d\sigma}(\dot{\sigma}_0\tau')$$
$$= \frac{4\pi^2}{\mu} \int_{-\infty}^{0} d\tau' \frac{d\Phi}{d\sigma}(\dot{\sigma}_0\tau') = \frac{4\pi^2\Phi(0)}{\dot{\sigma}_0\mu}. \qquad (24)$$

Here, we assume that the time during which the two particles interact is short compared to the periods of the chain modes, allowing us to replace $\dot{\Gamma}(-\tau') \to \dot{\Gamma}(0) = 2\pi$.

The displacement of the chain mass is approximately $\dot{\rho}(0)\tau_{\text{int}} \sim \Phi(0)\lambda_{\text{int}}/(\dot{\sigma}_0^2\mu)$, where $\tau_{\text{int}} \sim \lambda_{\text{int}}/\dot{\sigma}_0$ is the length of time during which the two particles interact and λ_{int} is the characteristic width of the interaction potential. Because the chain mass is confined by a potential well and springs connecting it to its neighbors, the potential energy associated with its displacement is approximately proportional to the displacement squared $\sim k_{\text{eff}}[\dot{\rho}(0)\tau_{\text{int}}]^2$. Here k_{eff} is an effective spring constant determined by k, κ, and μ. In our dimensionless formulation, we fix $\omega_{\min} = \sqrt{(\kappa/\mu)/K}$ and $\omega_{\max} = \sqrt{(4k/\mu)/K + (\kappa/\mu)/K}$, while allowing μ to change. Therefore, to vary the parameter μ, we must simultaneously vary k, κ, and hence k_{eff}, such that $k_{\text{eff}} \propto \mu$. Thus, the energy stored in the compressed spring is $\sim \mu[\dot{\rho}(0)\tau_{\text{int}}]^2$. This energy, originating from the moving particle, will be dissipated by the infinite chain and gives the energy loss of the mobile particle during a single pass: $\Delta\mathcal{E} \sim \mu[\Phi(0)\lambda_{\text{int}}]^2/(\dot{\sigma}_0^4\mu^2) \sim [\Phi(0)\lambda_{\text{int}}]^2/\mu\mathcal{E}^2$, where $\mathcal{E} = E/\hbar\Omega_M \sim \dot{\sigma}_0^2$. Because the frequency of the encounters between the two particles is virtually constant owing to the harmonic trap, the average energy-loss rate is given by $\dot{\mathcal{E}} \sim -\omega_M\Delta\mathcal{E} = -[\Phi(0)\lambda_{\text{int}}]^2/\mu\mathcal{E}^2$, which yields

$$\mathcal{E}(\tau) = \left[\mathcal{E}_0^3 - C\tau \frac{\Phi^2(0)\lambda_{\text{int}}^2}{\mu} \right]^{\frac{1}{3}}, \qquad (25)$$

where C is a numerical constant.

To illustrate the quasi-power-law behavior exhibited in Eq. (25), we perform a series of simulations for a range of potential widths λ and several values of μ in both attractive ($\Phi_0 < 0$) and repulsive ($\Phi_0 > 0$) regimes. We extract the coordinates of the turning points to obtain the time-dependent amplitude of the oscillations and plot the fractional amplitude reduction $1 - [\sigma(\tau)/\sigma_0]^6$ vs τ in Fig. 3. Based on the scaling argument above, the trajectory should have slope $+1$ on a log-log plot.

Figures 3(a)–3(c) demonstrate the scaling for the repulsive interaction for a set of parameters λ, μ, and $\Phi_0 > 0$. In addition to the turning points extracted from the simulations, we plot fits $1 - [\sigma(\tau)/\sigma_0]^6 = C\tau(\Phi_0\lambda)^2/\mu$ for $C = 7 \times 10^{-9}$. The fact that the same constant C yields good fits for a range of parameters supports our scaling argument. We see that for large $|\Phi_0|$ and λ the offset of the fits becomes worse. This deviation can be explained by the fact that wider (larger λ)
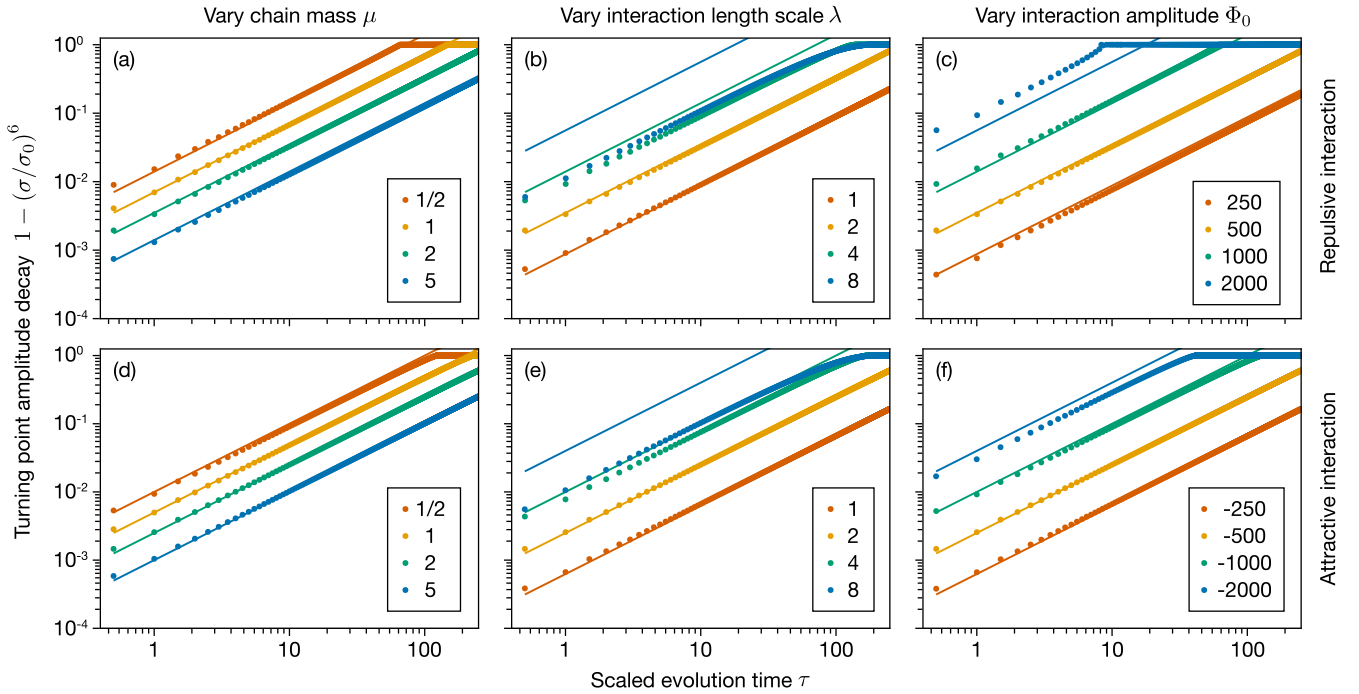
FIG. 3. *Scaling of amplitude decay.* The amplitude of the mobile particle at its turning points as a function of time shows a quasi-power-law behavior: $1 - [\sigma(\tau)/\sigma_0]^6 = C\tau(\Phi_0\lambda)^2/\mu$. The dots show data from the numerical simulations and the lines are fits. All the lines in the top (bottom) row have the same fit parameter $C = 7 \times 10^{-9}$ ($C = 5 \times 10^{-9}$) and slopes of $+1$ on the log-log axes. The fixed parameters for all the panels are $\omega_{\min} = 2$ and $\omega_{\max} = 20$. (a), (d) $\lambda = 2$, $\Phi_0 = \pm 500$; (b), (e) $\mu = 2$, $\Phi_0 = \pm 500$; (c), (f) $\mu = 2$, $\lambda = 2$.

and stronger (larger $|\Phi_0|$) potentials lead to longer interaction times τ_{int}. Consequently, the approximations used in deriving the scaling law become less appropriate. We obtain similar results for the attractive interaction, as shown in Figs. 3(d)–3(f). For the attractive potential, the best-fit value of the constant is smaller, $C = 5 \times 10^{-9}$.

The different values of C arise from the difference in effective interaction time between attractive and repulsive interactions. As an example, we consider the case of $\lambda = 2$ and $\mu = 2$, corresponding to the yellow data points in Figs. 3(b) and 3(e). Looking in detail at the first encounter between the mobile particle and the chain mass, we plot the displacement of the chain particle ρ and $-d\Phi/d\sigma$ for both signs of interaction in Fig. 4.

The interaction window is fairly short, amounting to about 8% of the mobile particle's travel time between turning points. Despite this short time, we see that the force and displacement curves are rather smooth, justifying our choice of time step in the calculations discussed in Sec. III B. Although the shapes of the force profiles that the chain mass trajectories are very similar between the attractive and repulsive interactions, we can see that the timescale is slightly longer and the maximum displacement of the chain mass is larger for the repulsive interaction. This difference is explained by the order of acceleration and deceleration that the mobile particle experiences. If the interaction is attractive, the mobile particle speeds up, being pulled forward by the chain mass, and then slows down as the chain particle "tugs"' on it. Conversely, if the interaction is repulsive, the mobile particle first experiences braking, followed by an acceleration. Consequently, the mobile particle moves slower when it passes the chain mass in the repulsive

configuration than it does in the attractive one, meaning that the effective contact time is larger in the repulsive case. The difference in the interaction time is directly related to the displacement of the chain particle and, therefore, the amount of elastic energy stored in the chain.
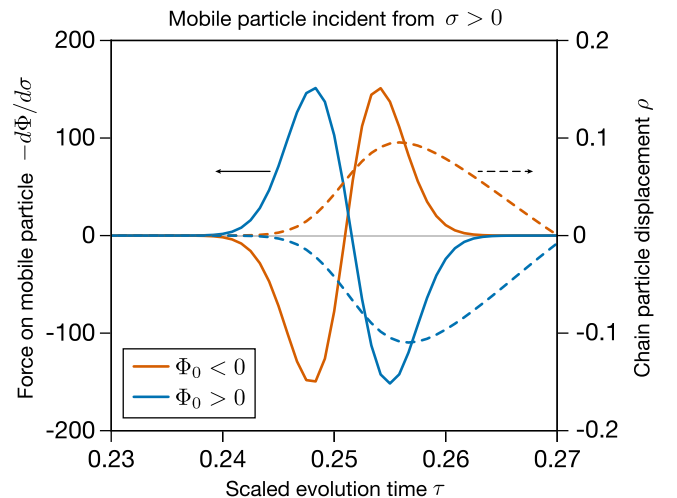

FIG. 4. *Difference between attractive and repulsive interactions.* Attractive and repulsive interactions with the same strength $|\Phi_0|$ and length scale λ lead to slightly different dynamics. A mobile particle incident from $\sigma > 0$ experiences a force with nearly identical profile (with opposite amplitude), but the displacement of the chain particle is slightly larger for repulsive interactions, and the duration is slightly longer. This extra displacement leads to slightly faster dissipation, as seen in Fig. 3. $\omega_{\min} = 2$, $\omega_{\max} = 20$, $\mu = 2$, $\lambda = 2$, $\Phi_0 = \pm 500$.
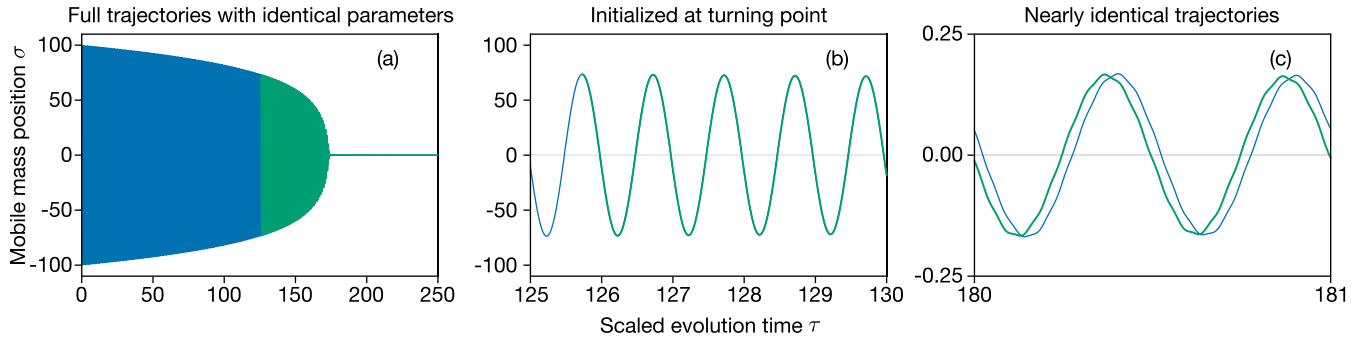
FIG. 5. *The role of history in dissipation.* A comparison of two trajectories for $\omega_{\min} = 2$, $\omega_{\max} = 20$, $\mu = 2$, $\lambda = 4$, and $\Phi_0 = -500$. The blue trajectory starts at $\sigma_0 = 100$ at $\tau = 0$ and the green one at $\sigma_0 \approx 73.5$ at $\tau \approx 126$. (a) An overlay of the two trajectories shows an identical envelope, magnified for a few oscillations in (b). (c) At later times, we see a mild disagreement in the dissipation-free regime.

C. Role of memory

Next, we discuss the impact of the memory term $\rho(\tau)$ on dissipative behavior through two calculations. We start by computing two particle trajectories with identical system parameters as in Fig. 2, but where the second particle is initialized at one of the later-time turning points of the first particle. This is equivalent to erasing the memory of the particle at that turning point. We plot the computed trajectories in Fig. 5 for $A_1 = 100$ and $A_2 \approx 73.5$. The calculations show that the large-amplitude trajectories for the two simulations coincide quite well. Only when the mobile particle falls into the potential well is there a noticeable difference between the two scenarios.

Based on this numerical experiment, we can see that the history of the trajectory in the large-amplitude regime has a minor effect on the motion of the particle. This result justifies our approach to the dissipation scaling in Sec. IV B, where we treated each encounter as independent from all the others. We might be tempted to conclude, based on this result, that the memory time plays a rather minor role in dissipation.

To investigate how dissipation is affected by the memory, we performed a series of calculations using the same parameters from Fig. 5, but including only the most recent segment of time τ_0. That is, we replaced the integral in Eq. (16) $\int_0^\tau \to \int_{\max(0, \tau - \tau_0)}^\tau$. In Fig. 6(a), we plot the amplitude decay for several values of the memory time, ranging from $\tau_0 = \infty$ to $\tau_0 = 1/20$. All of the trajectories exhibit nearly the same quasi-power-law scaling, with the largest deviation for $\tau_0 = 0.51$. Based on the specific value of τ_0, the dissipation can be either faster or slower than the $\tau = \infty$ case. Choosing a finite τ_0 leads to small countermovements in the position of the chain mass as it gradually "forgets" previous interactions. Due to the decaying behavior of $\Gamma(\tau)$, this behavior is especially prominent for short τ_0. For specific choices of $\tau_0 \approx 0.5, 1$, this motion can lead to pathological behavior as the countermovements occur during a subsequent interaction with the passing mobile particle. For certain system parameters, we found the dissipation for pathological τ_0 was qualitatively different from the $\tau_0 = \infty$ scaling. Obviously, a truncated memory kernel is rather artificial. While an ideal, isolated physical system should have $\tau_0 = \infty$, external couplings would lead to faster decay of the memory kernel $\Gamma(\tau)$. A suitable short memory

time shows similar behavior to $\tau_0 = \infty$, and also offers the benefit of easier calculation.

D. Multiple mobile particles

We also explore how the presence of multiple noninteracting mobile particles changes their dissipative dynamics. Initializing the positions of 25 mobile particles starting from rest with a mean position of 100 and standard deviation of 20, we tracked their resulting motion (see Appendix A for details). We found that each particle shows roughly the same quasi-power-law dissipation, with its timescale increased by the number of other particles "tethered" to the chain mass. For both attractive and repulsive interactions, the collection of mobile particles and the chain mass eventually exhibit persistent oscillations with frequencies just outside the phonon band, just as in the single-particle case.

V. THERMALIZATION

Having developed a good understanding of dissipation in our model system, we reintroduce the homogeneous thermal
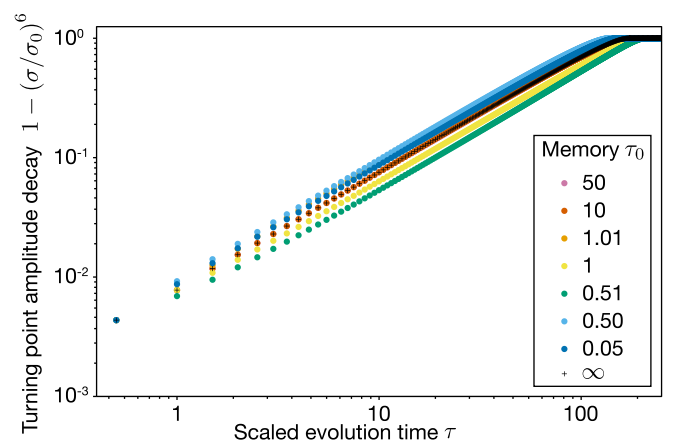

FIG. 6. *The role of memory in dissipation.* The amplitude reduction of the mobile particle at its turning points for $\omega_{\min} = 2$, $\omega_{\max} = 20$, $\mu = 2$, $\lambda = 4$, and $\Phi_0 = -500$ shows a relatively weak dependence on τ_0.

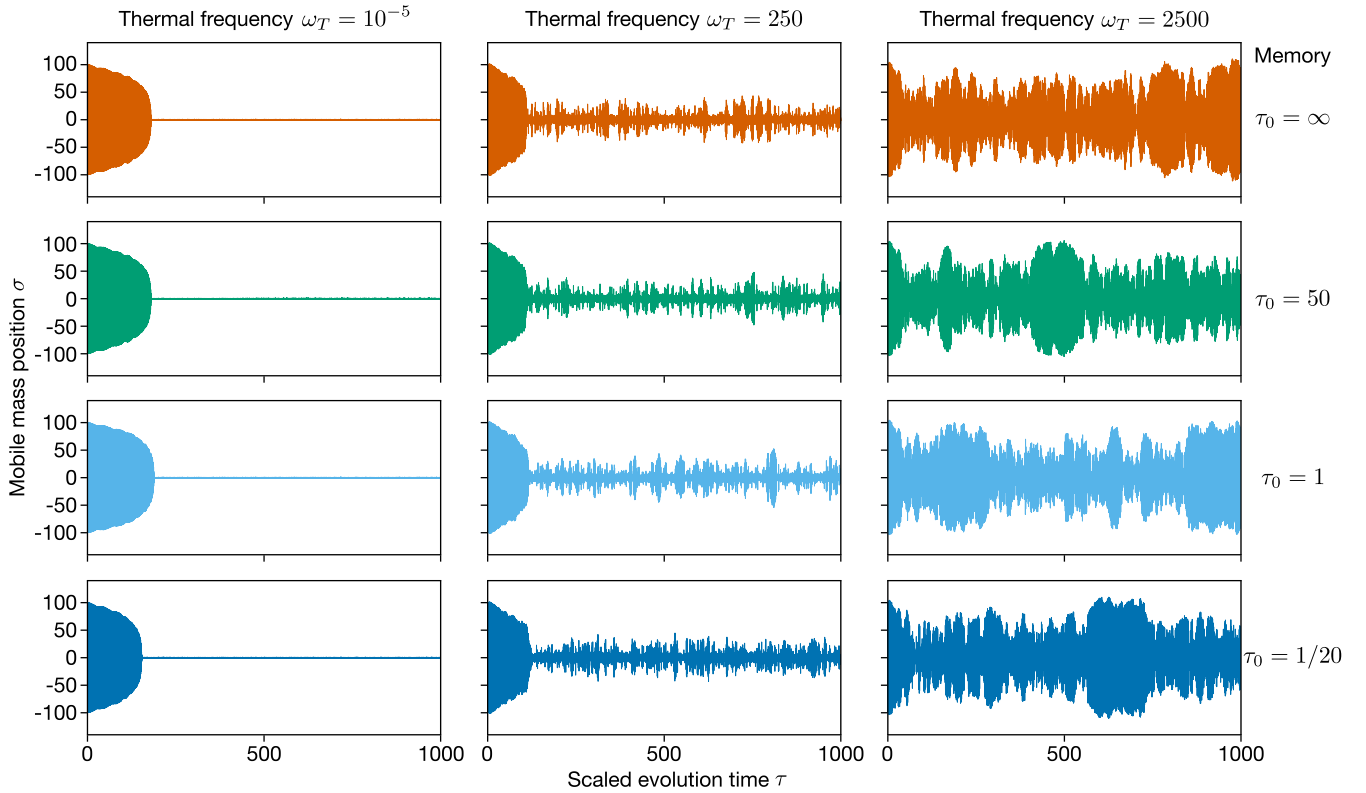FIG. 7. *General example with thermal motion included.* Trajectories of a single mobile particle $\sigma(\tau)$ for $\omega_{min} = 2$, $\omega_{max} = 20$, $\mu = 2$, $\lambda = 4$, $\Phi_0 = -500$ with $\sigma_0 = 100$ for three temperatures ω_T: 10^{-5} (left column), 250, (middle column), 2500 (right column) reveal dissipation and fluctuation. The four rows correspond to different memory times, from top to bottom: ∞, 50, 1, and 1/20.

motion term in Eq. (15). To justify our classical approach, we first verify that the vacuum fluctuations of the chain mass are much smaller than the characteristic interaction length λ:

$$\langle \rho^2 \rangle_{T=0} = \frac{1}{\mu\pi} \int_{\omega_{min}}^{\omega_{max}} \frac{dz}{\sqrt{z^2 - \omega_{min}^2}\sqrt{\omega_{max}^2 - z^2}}$$

$$= \frac{1}{\mu\pi} \frac{\mathcal{K}\left(1 - \frac{\omega_{min}^2}{\omega_{max}^2}\right)}{\omega_{max}} \approx \frac{1}{\mu\pi} \frac{\ln\left(\frac{4\omega_{max}}{\omega_{min}}\right)}{\omega_{max}}, \qquad (26)$$

where $\mathcal{K}(x)$ is the complete elliptic integral of the first kind. For the system parameters used above, $\mu = 2$, $\omega_{min} = 2$, $\omega_{max} = 20$, we find $\sqrt{\langle \rho^2 \rangle}_{T=0} \approx 0.17$. Lengths in our simulations are scaled by l_M, and the potential width $\lambda = 4$, so the scale of vacuum fluctuations is negligible.

A. Single particle

We start by computing individual particle trajectories with the same system parameters as in Fig. 2, but now including the $\rho^H(\tau)$ term in Eq. (18), calculated following the procedure given in Sec. III B. The results are shown in Fig. 7 for three different temperatures ($\omega_T = k_B T/E_M = 10^{-5}$, 250, and 2500, arranged in columns) and four different memory times ($\tau_0 = \infty$, 50, 1, and 1/20, arranged in rows). For a given temperature, the simulations with different memory times have identical $\rho^H(\tau)$.

As expected, increasing the temperature of the chain (going left to right in Fig. 7) produces a larger amplitude of the

mobile particle motion at later times. Although changing the memory time does alter the trajectory, the amplitude of the mobile particle motion remains nearly the same. Qualitatively, the trajectories for the particles at late times seem to only depend on the chain temperature. To quantitatively verify that these systems exhibit fluctuation behavior, we will study the statistical properties of the trajectory. We expect the mobile particle's energy distribution to be determined by the chain temperature. In particular, it should follow the Boltzmann distribution $P(E) \propto \exp(-\frac{E}{\hbar\Omega_T})$, or $P(\mathcal{E}) \propto \exp(-\mathcal{E}/\omega_T)$, where $\mathcal{E}$ is the total energy E of the mobile particle in units of E_M.

We repeat the calculations in Fig. 7 for a larger set of ω_T's: 100, 250, 500, 1000, and 2500 with the same four memory times using $\Phi_0 = \pm 500$. After calculating the trajectories, we extract the total energy $\mathcal{E}$ for the particle at each of the 1.2×10^6 time steps. In our dimensionless formulation, potential energy (in units of E_M) is given by $\sigma_{j,\alpha}^2/2 + \Phi(\rho_\alpha, \sigma_{j,\alpha})$, while the kinetic energy is $[(\sigma_{j,\alpha+1} - \sigma_{j,\alpha})/(2\pi\delta)]^2/2$. To eliminate the effects of the dissipative portion of the trajectory, we drop the first 10^5 steps for the repulsive potential and 1.5×10^5 for the attractive one (as we observed, the repulsive potential exhibits faster dissipation). Finally, we divide the energies by ω_T and build a normalized histogram to extract the probability distribution $P(\mathcal{E})$ as a function of $\mathcal{E}/\omega_T$. On a plot of $\ln[P(\mathcal{E})]$ vs $\mathcal{E}/\omega_T$, a particle at thermal equilibrium will have slope -1.

For the calculations in the top row of Fig. 8 (with repulsive interaction), we observe that the probability distributions mostly collapse onto a common line with a -1 slope, as expected. The deviation at low energies is due to the repulsive
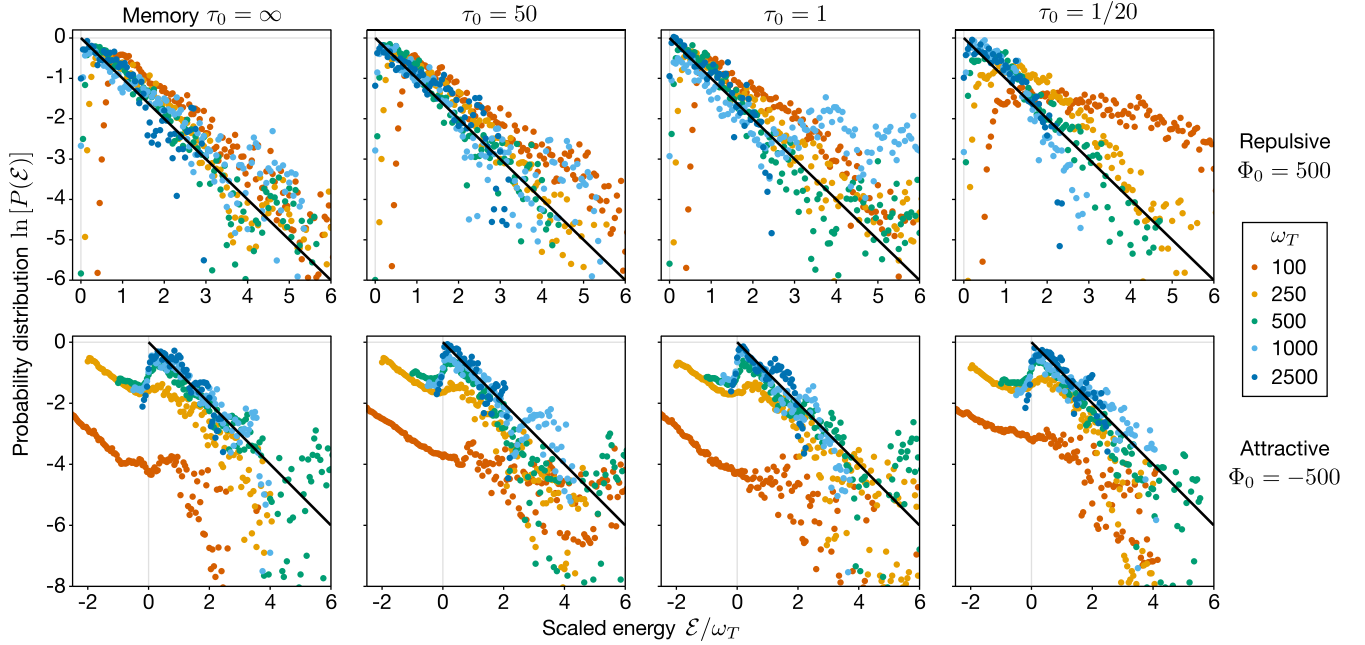
FIG. 8. *Energy probability distribution.* Logarithm of the probability distribution of total energy per particle $\mathcal{E}$ vs the total energy divided by the chain temperature ω_T for $\omega_{\min} = 2$, $\omega_{\max} = 20$, $\mu = 2$, $\lambda = 4$, and $\Phi_0 = \pm 500$. The top (bottom) row contains the results for repulsive (attractive) interactions. The four columns correspond, from left to right, to $\tau_0 = \infty$, 50, 1, and 1/20. The black lines each have a slope of -1, corresponding to the Boltzmann distribution $P = e^{-\frac{\mathcal{E}}{\omega_T}}$. The collapse of the data points onto the black curve indicates that the mobile particle follows the Boltzmann distribution with the same temperature as the chain.

interaction between the chain and the mobile particle, so that the latter never has zero energy. For larger ω_T, the time between interactions with the chain mass is longer, so our finite simulations undersample the rarer high-energy time steps. Unlike the dissipative case, a short memory time τ_0 can also give rise to pathological behavior, particularly for lower temperatures. In this case, the interactions between the mobile particle and chain mass become more frequent and take longer, so truncating the memory leads to problematic countermotion.

In the case of attractive interactions, shown in the bottom row of Fig. 8, we see that for sufficiently high ω_T's, we obtain the expected linear relationship between $\ln[P(\mathcal{E})]$ and $\mathcal{E}/\omega_T$. For lower ω_T's, however, there is a qualitatively different behavior for negative energies. In this regime, the mobile particle spends a significant fraction of time in very close proximity to the chain mass, essentially trapped in the interaction potential. Consequently, the mobile particle becomes tethered to the chain particle, and we do not expect it to exhibit the proper statistics.

For the repulsive case, where the mobile particle does not get as tightly tethered, another pathology arises. For low temperatures $\omega_T \lesssim \Phi_0$, the mobile particle will spend a large fraction of time near the chain mass. In this regime, the pathological countermotion produced by truncating the memory integral has a greater impact on the mobile particle's motion. Thus, shorter τ_0 can lead to anomalously high apparent temperatures, as seen in the top right panel of Fig. 8.

B. Multiple particles

To improve the statistics while also making the system more realistic, we also performed calculations with 25 mobile

particles, with identical system parameters as in Fig. 8. We initialized the particles starting from rest, positioned according to a normal distribution with a mean of 100 and standard deviation of 20. To make the comparison between different simulation runs more robust, we used the same starting positions by employing the same random seed.

To illustrate the rate of thermal equilibration, we plot the average energy per particle as a function of time for a repulsive potential in Fig. 9. Except in the case of $\omega_T = 50$,
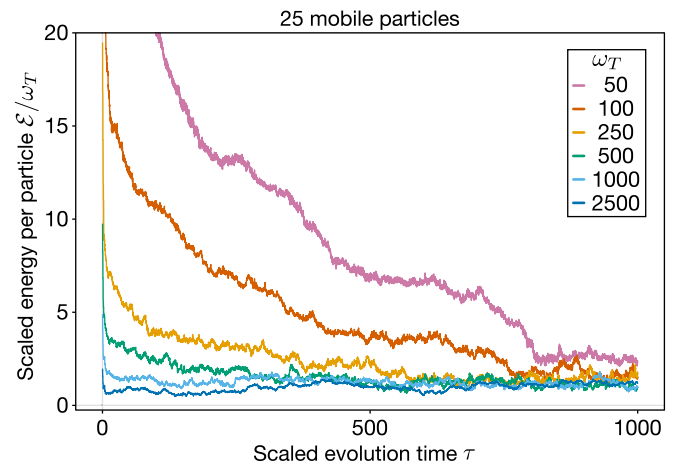

FIG. 9. *Thermal equilibration of mobile particles.* Average energy per mobile particle in an ensemble of 25 mobile particles for $\omega_{\min} = 2$, $\omega_{\max} = 20$, $\mu = 2$, $\lambda = 4$, and $\Phi_0 = 500$. The trajectories approach $\mathcal{E}/\omega_T = 1$ as the temperature of the particle ensemble approaches ω_T.
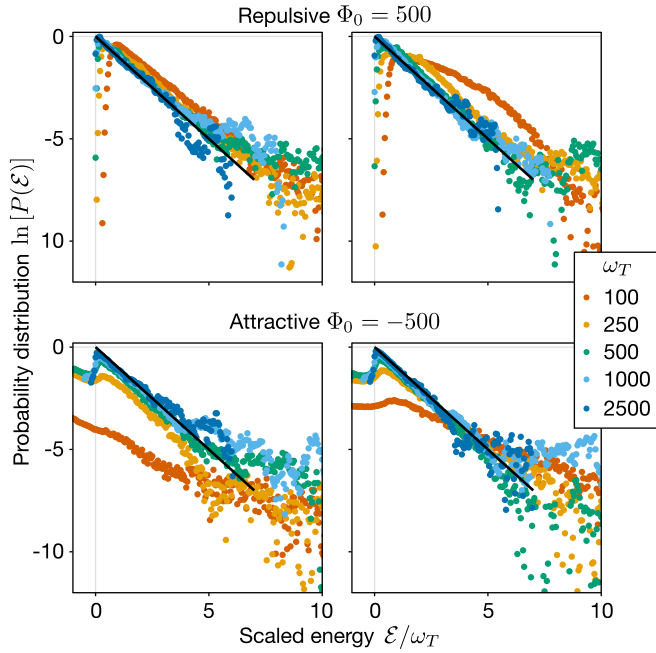
FIG. 10. *Energy probability distribution for an ensemble.* Logarithm of the probability distribution of total energy per particle vs the total energy per particle divided by the chain temperature ω_T for $\omega_{\min} = 2$, $\omega_{\max} = 20$, $\mu = 2$, $\lambda = 4$, and $\Phi_0 = \pm 500$ obtained from a simulation with 25 mobile particles. The top (bottom) row contains the results for repulsive (attractive) interactions. The left column corresponds to $\tau_0 = \infty$, and the right one to $\tau_0 = 1/20$. $\tau_0 = 1/20$ is essentially the Markovian limit, where the chain mass responds to the interaction with the mobile particle and "forgets" the interaction immediately after. The black lines have slopes of -1, corresponding to the Boltzmann distribution $P = e^{-\frac{\mathcal{E}}{\omega_T}}$.
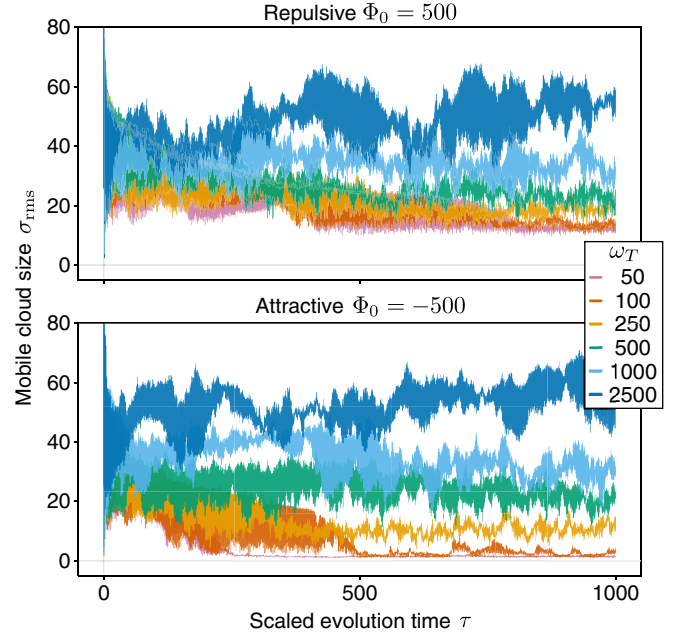

FIG. 11. *Cloud size.* Root-mean-square displacement of the mobile particles for repulsive (top) and attractive (bottom) interactions with the chain. The data are obtained from the simulations used to produce the left column of Fig. 10. The cloud size within the harmonic trap roughly matches the chain thermal energy scale $\sigma_{\mathrm{rms}}^2 \approx \omega_T$.

where the repulsive interaction potential substantially shifts the minimum attainable energy of the mobile particles, each of the ensembles eventually approaches thermal equilibrium $\mathcal{E} \to \omega_T$. We see that as ω_T increases, the equilibration time decreases substantially. Intuitively, this pattern makes sense, as the mobile particles dissipate more energy in the case of lower ω_T. We do not show results of similar calculations with an attractive potential because once the particles become tethered to the chain mass, their negative energy significantly skews the average.

Next, we construct the probability distribution of the total energy per particle, similar to Fig. 8, but for just two memory times $\tau_0 = \infty$, $1/20$. We expect that the addition of multiple mobile particles will reduce the effect of anomalous countermotion caused by truncating the memory. In the single-particle case, the countermotion was especially problematic because it tended to reverse the energy transfer of the previous interaction. In the many-particle case, however, the numerous intervening interactions tend to overwhelm the countermotion as the response to 24 other particles dwarfs the countermotion originating from a single contact. Put differently, from the point of view of a given particle, additional interactions conceal the countermotion by effectively adding randomness to the chain mass' trajectory. We see from the results in Fig. 10 that the 25-fold increase in the number

of data points improves the agreement with the Boltzmann distribution. We also observe that reducing the memory from infinity to $1/20$ does not substantially change the resulting distribution, except for at low temperatures.

Although we did not include any interaction between the mobile particles, they do, in fact, interact indirectly via the chain. To ensure that this interaction does not impact the individual particle statistics by giving rise to collective behavior, we found that the cross correlations of the particle positions are rather small (see Appendix B).

Naturally, raising the temperature of the system increases the oscillation amplitude of the mobile particles, leading to a larger cloud size. In a harmonic trap, the cloud size can be used as a proxy for the temperature. To illustrate this increase, we plot the root-mean-squared displacement σ_{rms} for a range of temperatures for both attractive and repulsive interactions in Fig. 11. We also investigate cloud heating by initializing the 25 particles normally distributed around the origin with a standard deviation of 1 and tracking the increase of σ_{rms} over time in Fig. 12. We see that the final σ_{rms} for different temperatures is the same regardless of the initial positions of the mobile particles.

C. No memory

Based on our simulations, we see thermalization for a wide range of memory times τ_0, even in the Markovian limit at $\tau_0 \to \tau_{\mathrm{int}}$, where τ_{int} is the typical particle-chain interaction time. Computationally, it is much simpler to eliminate the recoil term altogether, setting $\rho(\tau) = \rho^H(\tau)$. However, we find that in the absence of a recoil term, the mobile particles
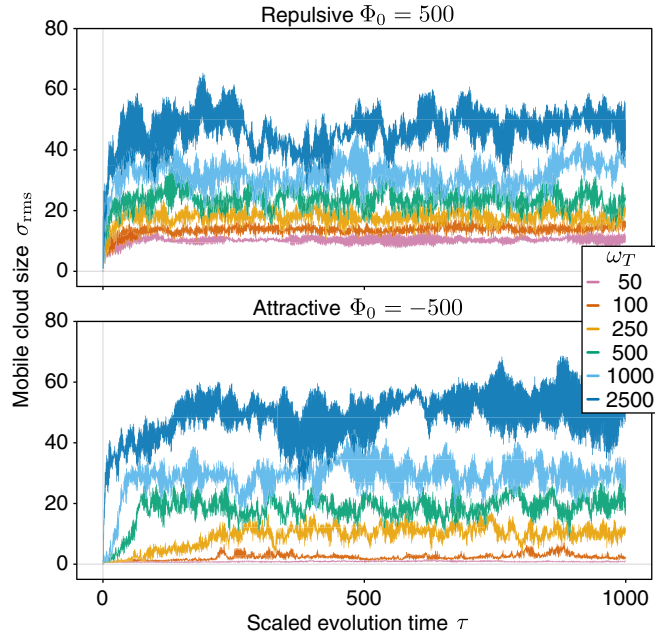
FIG. 12. *Cloud size increase*. Root-mean-square displacement of the mobile particles for the repulsive (top) and attractive (bottom) interaction with the chain. The system parameters are the same as in Fig. 11, but now the particles are initialized close to the bottom of the potential well. The final cloud size for each temperature and interaction agrees with the corresponding result from Fig. 11, indicating that the initial conditions do not play a role in determining the spread of the mobile particles. Again, the final cloud size within the harmonic trap roughly matches the chain thermal energy scale $\sigma_{rms}^2 \approx \omega_T$.

do not approach a Boltzmann distribution of energy, even after very long times, as seen in Fig. 13. In these simulations, the average energy per particle remains roughly constant, as seen in the insets, in contrast to the dissipation seen in Fig. 9. In practical terms, any experimental implementation of such a model requires some form of feedback to display thermalization.

VI. PROPOSED IMPLEMENTATIONS

Several experimental platforms for investigating 1D physics have arisen in the past few decades. Here we outline some candidate systems that could be used as realizations to validate the simple model we have developed. We discuss some of the technical hurdles of each platform, as well as possible avenues for extension.

A. Trapped ion and dimple potential

One of the most common trapping geometries for ions, the linear Paul trap, confines ions to motion in a 1D harmonic potential [27]. Another geometry using surface electrodes is emerging as a platform for quantum computing, and can be engineered to generate tunable potentials [28] or to couple to light [29]. In both trap geometries, it is possible to load a small number of ions, or even a single ion, into the trap. These trapped ions take the role of the mobile particle in our model
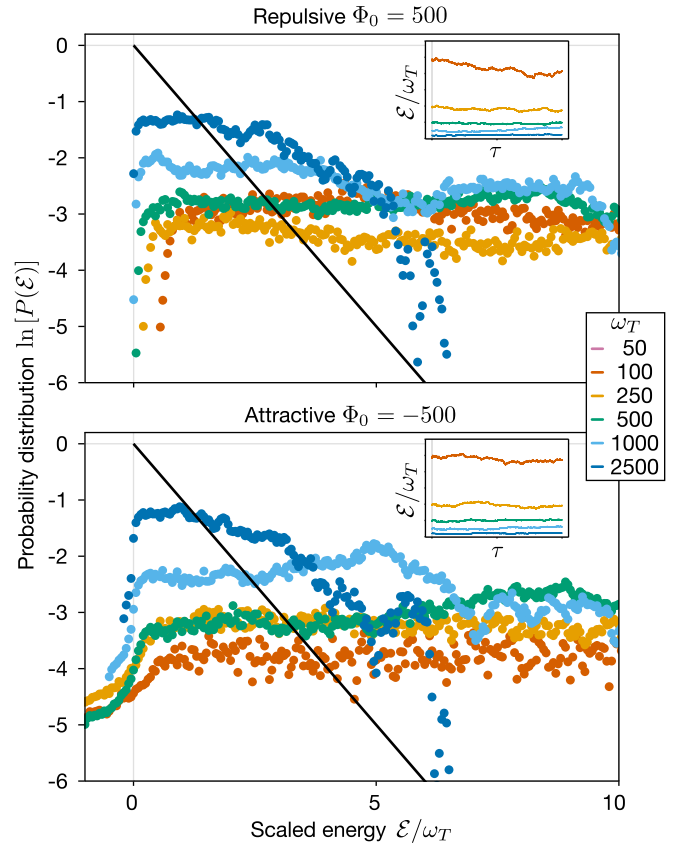

FIG. 13. *Simulations without memory*. Logarithm of the probability distribution of total energy per particle vs the total energy per particle divided by the chain temperature ω_T for the same parameters as in Fig. 10 but with $\tau_0 = 0$. The insets show the evolution of energy per particle with time. The lack of data collapse onto the Boltzmann distribution indicates the absence of thermalization.

since they move axially in a quasi-1D harmonic potential. Typical axial trap frequencies vary from several kHz [30] to the MHz regime [31], with motional heating rates as low as a few quanta/s at cryogenic temperatures [32]. In order to implement the effective bath coupling, the trap potential near the center could be modified using a small dc electrode or a tightly focused laser beam, which would produce a dimple potential [28,33].

By monitoring the position of the ion using a weak probe beam [34,35] or fluorescent light [36], the position and depth of the dimple could be modified with a feedback loop according to the dynamics described in Eq. (15). Similar feedback loops using large-scale electric fields produced by trap electrodes have been implemented in two main ways: cold damping [37] and parametric cooling [34].

In this implementation, adding multiple mobile ions to the trap is straightforward. However, the Coulomb coupling between mobile ions is much stronger than the effective bath coupling; we will explore this strongly interacting case in future work. In contrast to other cooling methods, our scheme only perturbs the trap locally. It could thus potentially be useful in contexts where the trap frequency needs to remain stable, such as in ion-based sensing.

B. Hybrid atom-ion system

Another experimental system that has been extensively studied recently consists of a small number of ions immersed in a cloud of neutral atoms [38,39]. These hybrid systems are useful for studying collision dynamics, or to use the ions as sensitive probes of the cloud [40,41]. In a typical implementation, an ion is confined using a Paul trap, with neutral atoms overlapped using optical potentials [42]. However, since the radio-frequency potential for the ion is much deeper than the optical trap experienced by the neutral atoms, the length scale for ion motion is smaller than the typical neutral cloud size. Recent experiments have employed optical traps for both the ion and the neutral cloud [43–45]. An ion confined to quasi-1D motion in an optical dipole trap that intersects a cloud of neutral atoms that are confined in a separate optical dipole trap could realize our model. The large number of degrees of freedom in the neutral cloud would let it serve as an effective bath that couples to the ion's secular motion via collisions at the trap center, where the neutral cloud's size and density would determine the parameters of the coupling λ, Φ_0. The initial kinetic energy of such an ion is on the order of 100 $\mu K/k_B$, and the temperature of a typical ultracold cloud is $\sim 1\,\mu K$.

Using a similar setup, but in another regime, where the ion undergoes many collisions with the neutral atoms, a similar damping effect occurs, known as buffer gas cooling [46–48]. One potential pitfall of this approach is that the ac Stark shift induced by the neutral cloud's trapping light will induce a static dimple in the ion's potential. This additional dimple could enhance or slow down the dissipation rate, depending on details of the trap laser. One way to circumvent this issue would be to trap the neutral cloud using a laser at a magic wavelength of the ion [49].

Similar to the ion and dimple approach, this platform can easily scale to multiple mobile particles, and the properties of the bath coupling can be tuned. For example, the neutral atom cloud size and density can be varied by changing the optical trap power, and its temperature can extend from the thermal to quantum regimes. We will explore the implications of a quantum bath in future work.

C. Neutral atom bright soliton and dimple

Another quasi-1D system with slow dynamics is bright solitons of bosonic neutral atoms in optical waveguides. Bright solitons have been implemented with several atomic species [50–54], and are commonly trapped in a far-detuned optical dipole potential which provides harmonic confinement. The lifetime of such solitons can be as high as 3 s, apparently limited by atom loss due to background collisions [51]. Several groups have also introduced optical dimple potentials [55–58], where the size of the dimple is usually $\gtrsim 2$ μm (smaller than a typical soliton size of ~ 10 μm) and the depth or height of the dimple can be tuned over four orders of magnitude [59].

The harmonic axial motion can be varied with a combination of magnetic fields and optical potentials from $\sim 5-100$ Hz. With nondestructive techniques, up to 50 images of a cloud can be acquired [60], allowing many oscillation periods of feedback.

This scheme, due to its long timescale for dynamics, would offer the easiest route toward imaging-based feedback, and would allow the most detailed exploration of feedback involving very short memory τ_0.

D. Neutral atoms in waveguide with dimple

A similar implementation involving quasi-1D motion of the mobile particles involves an optical waveguide, but with a large number of neutral atoms moving independently. This system has the same general setup as the soliton experiments above; however, the dynamics of the mobile particles will be complicated by two extra radial degrees of freedom. We suspect that a modulated dimple would dissipate energy from the axial motion, and weak interactions between the mobile atoms could lead to dissipation in all three dimensions. In the experiments described in [61] and further analyzed in [62], a sinusoidally modulated dimple beam leads to heating of a BEC. This type of modulation is closely related to Floquet engineering (for a review, see [63]). With some modifications to the experimental protocol, this system could load a thermal gas of atoms, observe the cloud density through nondestructive imaging, then change the dimple beam position based on Eq. (17), and measure the resulting distribution of kinetic energies in the cloud through standard time-of-flight imaging.

E. Neutral atoms in an optical lattice with dimple

To restrict the motion of the mobile atoms more closely to 1D, they could be confined using a two-dimensional (2D) optical lattice. Around 20–100 atoms would undergo harmonic motion in each of the ~ 1000 1D tubes, with Ω_M tunable from $\sim 1-1000$ Hz. For a strong enough optical lattice, the energy scale of transverse motion ~ 100 kHz could be tuned far above other energy scales in the system. A light sheet focused very tightly along the axis of the atoms' motion could produce a dimple trap with uniform depth across all of the 1D tubes, yielding many independent realizations of our model system.

One of the major challenges of this approach is implementing the feedback necessary to observe dissipation. Inhomogeneities would lead to slightly different Ω_M in each of the tubes, precluding effective feedback with a single dimple potential. To make the system more uniform, the optical lattice depth could be tuned using optical techniques [64].

F. Neutral atoms and optical cavity

An experimental tool that could more directly probe the effects of the bath modes in our simulations is an optical cavity. If a multimode cavity [65] were aligned transverse to an optical waveguide, the moving atoms would couple to the cavity modes only near the center of the trap. The cavity length could be chosen to tune the energy scale of cavity modes ($\omega_{\min}$, $\omega_{\max}$ in our model) relative to the kinetic energy of the mobile particles.

The cavity modes could potentially also be populated in a controlled way to emulate different chain temperatures (or nonequilibrium states). These modes might even be controllable in a feedback loop similar to [66].

VII. CONCLUSION

Using a simple model of mobile particles in a harmonic potential coupled to a 1D chain of masses, we have demonstrated both dissipation and fluctuation behaviors using classical numerical simulations. In the absence of thermal fluctuations, individual particles dissipate energy in a quasi-power-law fashion, with a characteristic time that generally follows a simple scaling based on system parameters. With multiple noninteracting mobile particles, each of them dissipates energy, with a timescale determined by the number of particles already lying near the chain mass.

Once thermal fluctuations are introduced in the chain motion, we find behavior reminiscent of thermal equilibration. First, as long as the mobile particles are not trapped in the interaction potential, they approach a Boltzmann distribution of energy, set by the temperature of the chain. Next, the characteristic size of a cloud of mobile particles in the harmonic potential eventually matches the thermal energy scale of the chain as well. For all reasonable choices of the memory time, the system exhibits the same thermalizing behavior. In contrast, with no memory, the mobile particles' motion is not strongly influenced by the chain, and does not reach a Boltzmann distribution.

We showed that this minimal system exhibits fluctuation and dissipation behavior for a wide range of system parameters. We suspect that the specific form of the chain-particle interaction has little effect on the resulting dynamics. However, for some specific interactions, such as a delta-function potential, a different numerical approach will be necessary. We also suspect that the mode structure of the chain has no qualitative impact on the mobile particle trajectories, and will explore this claim in future work.

We proposed several experimental platforms where this minimal setup could be realized, though each introduces some potential complications. To model more realistic systems, we will explore the case where the mobile particles interact with one another in future work. We will also explore how multiple couplings to the chain affect the resulting dynamics. In this case, the harmonic confinement can be removed, and we expect to observe signatures of diffusion of the mobile particles, in addition to dissipative behavior. This modification will allow us to explore indirect interactions between mobile particles mediated by the chain. Additionally, we can explore the appearance of friction and extract the effective friction coefficient. Another natural extension is to modify the structure of the bulk by either altering the phonon dispersion or by increasing the dimensionality of the system. Specifically, the larger number of phonon modes in higher dimensions should lead to faster dephasing, making the memory less important. In several of the proposed implementations, the scales of the system approach the quantum regime, which will require significant modifications to our approach.

More broadly, this work is a step in developing our understanding of drag and diffusion in solid systems in a non-Brownian regime with nonlinear interactions. By formulating the problem using microscopic ingredients, we are able to explore the validity of the approximations commonly employed in diffusion problems in solid systems. From a practical standpoint, improved understanding of dissipative processes in solid materials has a direct impact on our ability to design efficient ionic conductors required for the fabrication of solid-state batteries.

APPENDIX A: MULTIPARTICLE DISSIPATION

To explore how a collection of particles dissipates energy via their interaction with a single chain mass (with no thermal fluctuations), we introduce 25 mobile particles starting from rest with a mean position of 100 and standard deviation of 20. The trajectories of the mobile particles are plotted simultaneously along with the chain mass for both attractive and repulsive interactions in Fig. 14.

For attractive interactions, similar to the single-particle case, the mobile particles settle near the chain mass, reaching $|\sigma_j - \rho| \approx 1$ one by one. Individual particles show qualitatively similar dissipation, roughly following quasi-power-law trajectories. After each particle dissipates most of its energy, the collection of masses then oscillates with a persistent amplitude, similar to the behavior seen in Fig. 2.

The motion of the chain mass in this regime exhibits two modes which lie further outside the phonon band than the ones observed in Fig. 2. Following the steps leading to Eq. (20), we obtain that $\rho_\omega = \frac{\Phi_0}{\mu\lambda^2} f_\omega \sum_j (\sigma_{j,\omega} - \rho_\omega)$ and $(1 - \omega^2 - \frac{\Phi_0}{\lambda^2})\sigma_{j,\omega} + \frac{\Phi_0}{\lambda^2}\rho_\omega = 0$, where $j \in [1, P]$ runs over the mobile particles in the Gaussian well, leading to

$$
\begin{pmatrix}
1 - \omega^2 - \frac{\Phi_0}{\lambda^2} & 0 & \cdots & \frac{\Phi_0}{\lambda^2} \\
0 & 1 - \omega^2 - \frac{\Phi_0}{\lambda^2} & \cdots & \frac{\Phi_0}{\lambda^2} \\
\vdots & \vdots & \ddots & \vdots \\
-\frac{\Phi_0}{\lambda^2} f_\omega & -\frac{\Phi_0}{\lambda^2} f_\omega & \cdots & 1 + P\frac{\Phi_0}{\lambda^2} f_\omega
\end{pmatrix}
\begin{pmatrix}
\sigma_{1,\omega} \\
\sigma_{2,\omega} \\
\vdots \\
\rho_\omega
\end{pmatrix}
$$
$$
= 0. \tag{A1}
$$

Taking the determinant of the matrix and setting it equal to zero yields $(P - 1)$-degenerate modes with $\omega = \sqrt{1 - \frac{\Phi_0}{\lambda^2}}$ and two more modes with frequencies obtained by solving

$$
(1 - \omega^2)\left(1 + P\frac{f_\omega \Phi_0}{\mu\lambda^2}\right) = \frac{\Phi_0}{\lambda^2}. \tag{A2}
$$

For the degenerate solutions, the system parameters yield $\omega \approx 5.68$, which lies within the phonon band. As such, this solution will give rise to decaying oscillations, in accordance with Eq. (20). Solving Eq. (A2) for $P = 24$, we get two solutions: one with $\omega \approx 1.65$ and the other with $\omega \approx 25.4$. This prediction is borne out in our simulations, as seen in Fig. 14(c)
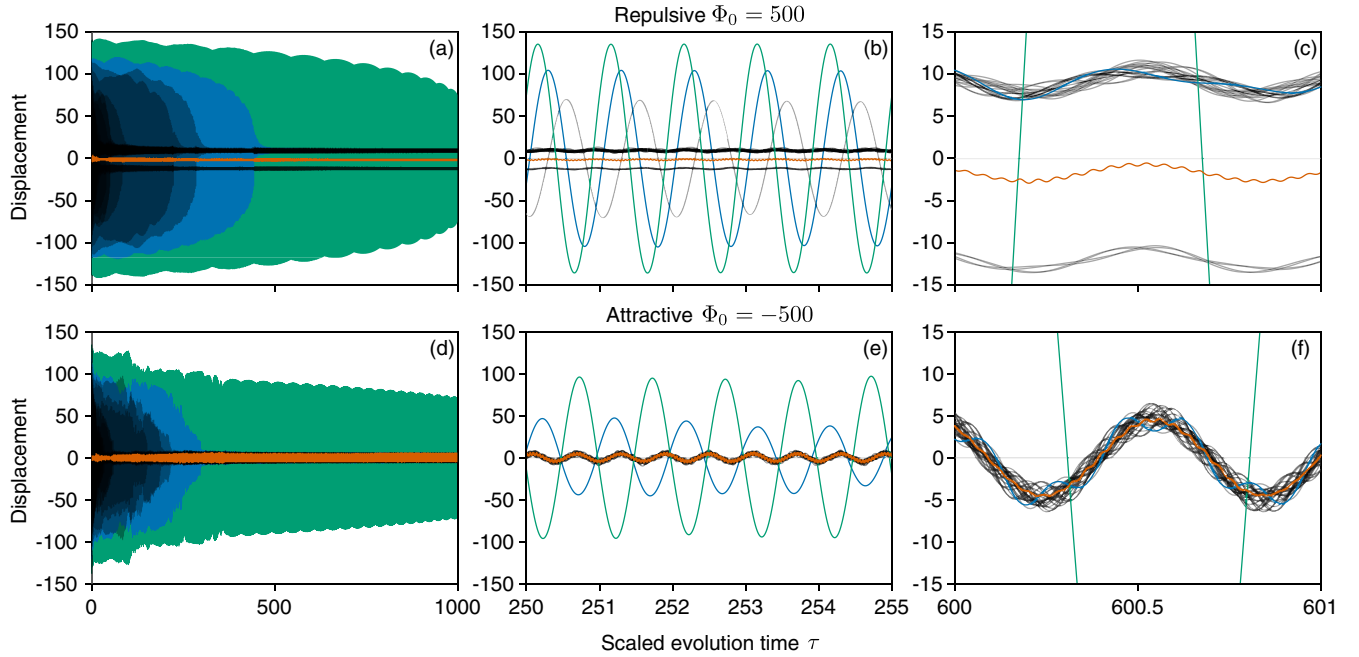
FIG. 14. *Dissipation for a collection of particles.* 25 particles are initialized from rest following a normal distribution with mean of 100 and standard deviation of 20. The system parameters are $\omega_{\min} = 2$, $\omega_{\min} = 20$, $\mu = 2$, $\lambda = 4$, and $\Phi_0 = \pm 500$, with the top (bottom) row corresponding to repulsive (attractive) interaction. The initial positions for the mobile particles are the same for both simulations.

by counting the fast and slow oscillations. As before, because the two frequencies lie outside the phonon band, the energy is not dissipated. Increasing P further pushes the ω's away from the phonon band.

For the repulsive case, the situation is somewhat more complex. Some of the mobile particles settle on the left side of the chain mass, while the rest settle on the right, confined on one side by the chain mass and on the other by the harmonic potential. The equilibrium positions depend on the exact split of the particles between left and right and determining their locations requires solving transcendental equations. Moreover, the equivalent of Eq. (19) for the repulsive case is substantially more complicated when multiple particles are involved. Hence, we do not perform a detailed analysis for the repulsive case. Instead, we simply demonstrate the presence of persistent oscillations for the repulsive case in the bottom row of Fig. 14.

We observe that, unlike the single-particle simulations, the dissipation for the repulsive interaction is not faster than the attractive one. Given that in the single-particle case the difference in the dissipation rate between the two signs came from a slightly longer effective interaction time for the repulsive interaction, this effect is easily disrupted in the presence of multiple mobile particles. A closer look reveals that the repulsive interaction actually exhibits slower dissipation. The reason behind this difference is the uneven deposition of the mobile particles on the two sides of the chain mass. In the attractive case, the mobile particles that have fallen into the Gaussian well are distributed without any particular order with respect to the chain mass, as can be seen from Fig. 14. Conse-

quently, they do not substantially impede the minute motion of the chain mass in response to the fast-moving nontethered particles. For the repulsive potential, on the other hand, more mobile particles may settle on the positive side of the chain mass than on the negative. Because of the uneven distribution, the chain mass' energy minimum is slightly to the left of zero. As a result, the motion of the chain mass is restricted by the mobile masses on one side and by the compressed κ spring on the other. This increased confinement reduces the ability of the chain mass to move, reducing its dissipation ability.

APPENDIX B: CORRELATIONS

To assess the validity of treating the mobile particles in the ensemble as independent, we calculate the position correlations for all the runs in the left column of Fig. 10. We then average the 25 autocorrelation and 600 cross-correlation functions for each ω_T and Φ_0 and plot the results in Fig. 15. We observe that the autocorrelation functions exhibit an expected decaying behavior, with the decay rate generally being slower for higher temperatures. This decay rate dependence on temperature can be attributed to a larger speed with which the mobile particles pass the chain mass, leading to a smaller perturbation. The cross-correlation are much smaller than the autocorrelations. The only exception is the lowest temperature for the attractive interaction, where the mobile particles fall into the Gaussian well and oscillate together. The small magnitude of the cross-correlation in the relevant simulation run warrants the treatment of the mobile particles as independent.
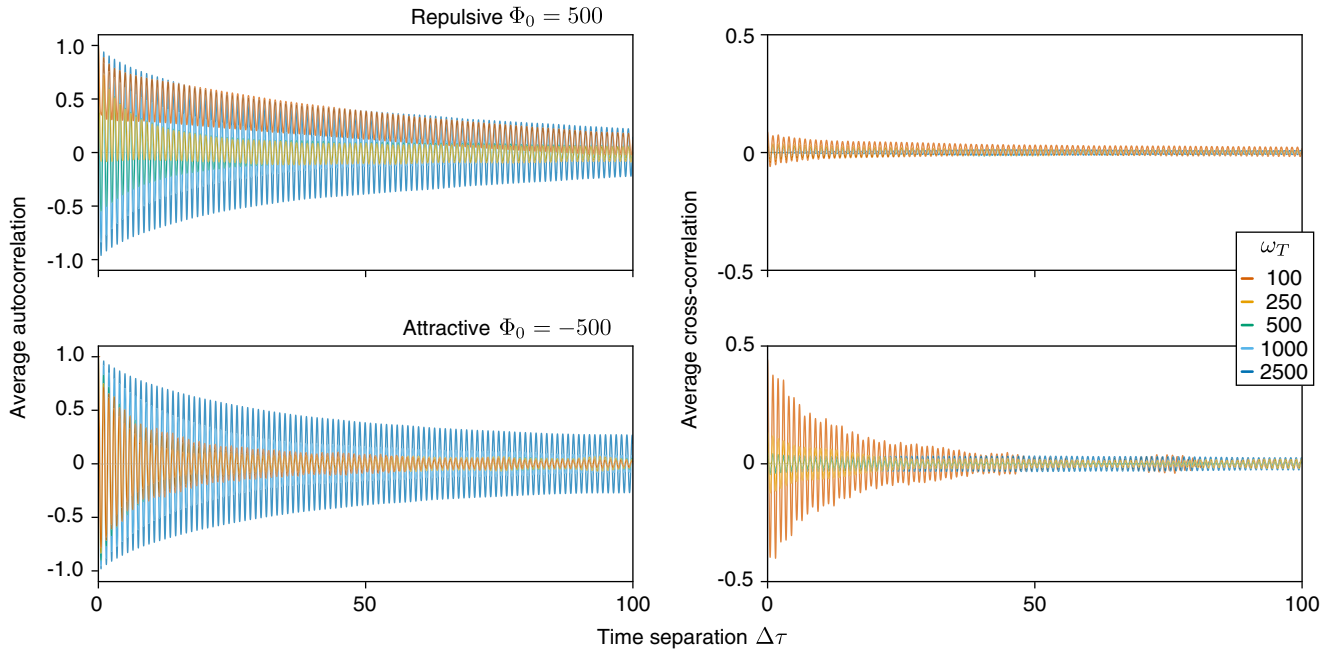
FIG. 15. *Correlation functions of a multiparticle ensemble.* Using the data employed to generate the left column in Fig. 10, we calculate correlations between all the particle trajectories for every run. The autocorrelation plots are obtained by averaging 25 autocorrelations for each run, while the cross-correlation are the averages of the 600 cross-correlation. The autocorrelation exhibits a decaying oscillatory behavior with the decay being the consequence of the chain-induced perturbation. The autocorrelation for repulsive interaction at low temperatures does not change sign because the mobile particle never passes to the other side of the chain mass.

[1] H. B. Callen and T. A. Welton, Irreversibility and generalized noise, Phys. Rev. **83**, 34 (1951).

[2] A. Einstein, Ìber die von der molekularkinetischen theorie der wärme geforderte bewegung von in ruhenden flüssigkeiten suspendierten teilchen, Ann. Phys. (Berlin, Ger.) **322**, 549 (1905).

[3] M. von Smoluchowski, Zur kinetischen theorie der brownschen molekularbewegung und der suspensionen, Ann. Phys. (Berlin, Ger.) **326**, 756 (1906).

[4] R. Brown, XXVII. A brief account of microscopical observations made in the months of June, July and August 1827, on the particles contained in the pollen of plants; and on the general existence of active molecules in organic and inorganic bodies, Philos. Mag. **4**, 161 (1828).

[5] P. Pearle, B. Collett, K. Bart, D. Bilderback, D. Newman, and S. Samuels, What Brown saw and you can too, Am. J. Phys. **78**, 1278 (2010).

[6] J. C. Bachman, S. Muy, A. Grimaud, H. H. Chang, N. Pour, S. F. Lux, O. Paschos, F. Maglia, S. Lupart, P. Lamp, L. Giordano, and Y. Shao-Horn, Inorganic Solid-State Electrolytes for Lithium Batteries: Mechanisms and Properties Governing Ion Conduction, Chem. Rev. **116**, 140 (2016).

[7] A. Manthiram, X. Yu, and S. Wang, Lithium battery chemistries enabled by solid-state electrolytes, Nat. Rev. Mater. **2**, 16103 (2017).

[8] T. Famprikis, P. Canepa, J. A. Dawson, M. S. Islam, and C. Masquelier, Fundamentals of inorganic solid-state electrolytes for batteries, Nat. Mater. **18**, 1278 (2019).

[9] A. Rodin, K. Noori, A. Carvalho, and A. H. C. Neto, Microscopic theory of ionic motion in solids, Phys. Rev. B **105**, 224310 (2022).

[10] R. P. Feynman and F. L. Vernon, The theory of a general quantum system interacting with a linear dissipative system, Ann. Phys. **24**, 118 (1963).

[11] A. J. Bray and M. A. Moore, Influence of Dissipation on Quantum Coherence, Phys. Rev. Lett. **49**, 1545 (1982).

[12] A. O. Caldeira and A. H. Castro Neto, Motion of heavy particles coupled to fermionic and bosonic environments in one dimension, Phys. Rev. B **52**, 4198 (1995).

[13] M. Schecter, A. Kamenev, D. M. Gangardt, and A. Lamacraft, Critical Velocity of a Mobile Impurity in One-Dimensional Quantum Liquids, Phys. Rev. Lett. **108**, 207001 (2012).

[14] S. Peotta, D. Rossini, M. Polini, F. Minardi, and R. Fazio, Quantum Breathing of an Impurity in a One-Dimensional Bath of Interacting Bosons, Phys. Rev. Lett. **110**, 015302 (2013).

[15] A. S. Dehkharghani, A. G. Volosniev, and N. T. Zinner, Quantum impurity in a one-dimensional trapped Bose gas, Phys. Rev. A **92**, 031601(R) (2015).

[16] A. Petković and Z. Ristivojevic, Dynamics of a Mobile Impurity in a One-Dimensional Bose Liquid, Phys. Rev. Lett. **117**, 105301 (2016).

[17] A. Castro Neto and M. P. A. Fisher, Dynamics of a heavy particle in a Luttinger liquid, Phys. Rev. B **53**, 9713 (1996).

[18] M. Pasek and G. Orso, Induced pairing of fermionic impurities in a one-dimensional strongly correlated Bose gas, Phys. Rev. B **100**, 245419 (2019).

[19] A. Lampo, S. H. Lim, M. Á. García-March, and M. Lewenstein, Bose polaron as an instance of quantum Brownian motion, Quantum **1**, 30 (2017).

[20] A. Petković, Microscopic theory of the friction force exerted on a quantum impurity in one-dimensional quantum liquids, Phys. Rev. B **101**, 104503 (2020).

[21] G. P. Berman and F. M. Izrailev, The fermi-pasta-ulam problem: Fifty years of progress, Chaos: An Interdisciplinary Journal of Nonlinear Science **15**, 015104 (2005).

[22] G. Gallavotti, *The Fermi-Pasta-Ulam Problem: A Status Report* (Springer, Berlin, 2008), p. 301.

[23] J. Bezanson, A. Edelman, S. Karpinski, and V. B. Shah, Julia: A Fresh Approach to Numerical Computing *, SIAM Rev. **59**, 65 (2017).

[24] https://github.com/rodin-physics/1d-parabolic-trap-thermalization.

[25] S. Danisch and J. Krumbiegel, Makie.jl: Flexible high-performance data visualization for julia, J. Open Source Software **6**, 3349 (2021).

[26] B. Wong, Points of view: Color blindness, Nat. Methods **8**, 441 (2011).

[27] A. Bylinskii, D. Gangloff, and V. Vuleti, Tuning friction atom-by-atom in an ion-crystal simulator, Science **348**, 1115 (2015).

[28] Z. D. Romaszko, S. Hong, M. Siegele, R. K. Puddy, F. R. Lebrun-Gallagher, S. Weidt, and W. K. Hensinger, Engineering of microfabricated ion traps and integration of advanced on-chip features, Nat. Rev. Phys. **2**, 285 (2020).

[29] M. Ivory, W. J. Setzer, N. Karl, H. McGuinness, C. DeRose, M. Blain, D. Stick, M. Gehl, and L. P. Parazzoli, Integrated Optical Addressing of a Trapped Ytterbium Ion, Phys. Rev. X **11**, 041033 (2021).

[30] A. D. West, R. Putnam, W. C. Campbell, and P. Hamilton, Tunable transverse spin-motion coupling for quantum information processing, Quantum Sci. Technol. **6**, 024003 (2021).

[31] C. D. Bruzewicz, J. M. Sage, and J. Chiaverini, Measurement of ion motional heating rates over a range of trap frequencies and temperatures, Phys. Rev. A **91**, 041402(R) (2015).

[32] J. Chiaverini and J. M. Sage, Insensitivity of the rate of ion motional heating to trap-electrode material over a large temperature range, Phys. Rev. A **89**, 012318 (2014).

[33] R. He, J.-M. Cui, R.-R. Li, Z.-H. Qian, Y. Chen, M.-Z. Ai, Y.-F. Huang, C.-F. Li, and G.-C. Guo, An ion trap apparatus with high optical access in multiple directions, Rev. Sci. Instrum. **92**, 073201 (2021).

[34] C. Sames, C. Hamsen, H. Chibani, P. A. Altin, T. Wilk, and G. Rempe, Continuous parametric feedback cooling of a single atom in an optical cavity, Phys. Rev. A **97**, 053404 (2018).

[35] P. Bushev, G. Héetet, L. Slodička, D. Rotter, M. A. Wilson, F. Schmidt-Kaler, J. Eschner, and R. Blatt, Shot-Noise-Limited Monitoring and Phase Locking of the Motion of a Single Trapped Ion, Phys. Rev. Lett. **110**, 133602 (2013).

[36] G. Cerchiari, G. Araneda, L. Podhora, L. S. Slodička, Y. Colombe, and R. Blatt, Measuring Ion Oscillations at the Quantum Level with Fluorescence Light, Phys. Rev. Lett. **127**, 063603 (2021).

[37] P. Bushev, D. Rotter, A. Wilson, F. Dubin, C. Becher, J. Eschner, R. Blatt, V. Steixner, P. Rabl, and P. Zoller, Feedback Cooling of a Single Trapped Ion, Phys. Rev. Lett. **96**, 043003 (2006).

[38] A. Härter and J. Hecker Denschlag, Cold atom-ion experiments in hybrid traps, Contemp. Phys. **55**, 33 (2014).

[39] M. Tomza, K. Jachymski, R. Gerritsma, A. Negretti, T. Calarco, Z. Idziaszek, and P. S. Julienne, Cold hybrid ion-atom systems, Rev. Mod. Phys. **91**, 035001 (2019).

[40] C. Veit, N. Zuber, O. Herrera-Sancho, V. S. V. Anasuri, T. Schmid, F. Meinert, R. Loöw, and T. Pfau, Pulsed Ion Mi-

croscope to Probe Quantum Gases, Phys. Rev. X **11**, 011036 (2021).

[41] M. Cetina, M. Jag, R. S. Lous, I. Fritsche, J. T. M. Walraven, R. Grimm, J. Levinsen, M. M. Parish, R. Schmidt, M. Knap, and E. Demler, Ultrafast many-body interferometry of impurities coupled to a Fermi sea, Science **354**, 96 (2016).

[42] S. Schmid, A. Haärter, and J. H. Denschlag, Dynamics of a Cold Trapped Ion in a Bose-Einstein Condensate, Phys. Rev. Lett. **105**, 133202 (2010).

[43] P. Weckesser, F. Thielemann, D. Wiater, A. Wojciechowska, L. Karpa, K. Jachymski, M. Tomza, T. Walker, and T. Schaetz, Observation of Feshbach resonances between a single ion and ultracold atoms, Nature **600**, 429 (2021).

[44] J. Schmidt, P. Weckesser, F. Thielemann, T. Schaetz, and L. Karpa, Optical Traps for Sympathetic Cooling of Ions with Ultracold Neutral Atoms, Phys. Rev. Lett. **124**, 053402 (2020).

[45] P. Weckesser, F. Thielemann, D. Hoenig, A. Lambrecht, L. Karpa, and T. Schaetz, Trapping, shaping, and isolating of an ion Coulomb crystal via state-selective optical potentials, Phys. Rev. A **103**, 013112 (2021).

[46] R. G. DeVoe, Power-Law Distributions for a Trapped Ion Interacting with a Classical Buffer Gas, Phys. Rev. Lett. **102**, 063001 (2009).

[47] Z. Meir, T. Sikorsky, R. Ben-shlomi, N. Akerman, Y. Dallal, and R. Ozeri, Dynamics of a Ground-State Cooled Ion Colliding with Ultracold Atoms, Phys. Rev. Lett. **117**, 243401 (2016).

[48] T. Feldker, H. Fürst, H. Hirzler, N. V. Ewald, M. Mazzanti, D. Wiater, M. Tomza, and R. Gerritsma, Buffer gas cooling of a trapped ion to the quantum regime, Nat. Phys. **16**, 413 (2020).

[49] J. Kaur, S. Singh, B. Arora, and B. K. Sahoo, Magic wavelengths in the alkaline-earth-metal ions, Phys. Rev. A **92**, 031402(R) (2015).

[50] L. Khaykovich, F. Schreck, G. Ferrari, T. Bourdel, J. Cubizolles, L. D. Carr, Y. Castin, and C. Salomon, Formation of a Matter-Wave Bright Soliton, Science **296**, 1290 (2002).

[51] K. E. Strecker, G. B. Partridge, A. G. Truscott, and R. G. Hulet, Bright matter wave solitons in Bose–Einstein condensates, New J. Phys. **5**, 73 (2003).

[52] S. L. Cornish, S. T. Thompson, and C. E. Wieman, Formation of Bright Matter-Wave Solitons during the Collapse of Attractive Bose-Einstein Condensates, Phys. Rev. Lett. **96**, 170401 (2006).

[53] S. Lepoutre, L. Fouchee, A. Boissé, G. Berthet, G. Salomon, A. Aspect, and T. Bourdel, Production of strongly bound K 39 bright solitons, Phys. Rev. A **94**, 053626 (2016).

[54] T. Mežnaršič, T. Arh, J. Brence, J. Pišljar, K. Gosar, Ž. Gosar, R. Žitko, E. Zupanič, and P. Jeglič, Cesium bright matter-wave solitons and soliton trains, Phys. Rev. A **99**, 033625 (2019).

[55] G. D. McDonald, C. C. N. Kuhn, K. S. Hardman, S. Bennetts, P. J. Everitt, P. A. Altin, J. E. Debs, J. D. Close, and N. P. Robins, Bright Solitonic Matter-Wave Interferometer, Phys. Rev. Lett. **113**, 013002 (2014).

[56] J. H. V. Nguyen, D. Luo, and R. G. Hulet, Formation of matter-wave soliton trains by modulational instability, Science **356**, 422 (2017).

[57] A. L. Marchant, T. P. Billam, T. P. Wiles, M. M. H. Yu, S. A. Gardiner, and S. L. Cornish, Controlled formation and reflection of a bright solitary matter-wave, Nat. Commun. **4**, 1865 (2013).

[58] O. J. Wales, A. Rakonjac, T. P. Billam, J. L. Helm, S. A. Gardiner, and S. L. Cornish, Splitting and recombination

of bright-solitary-matter waves, Commun. Phys. **3**, 51 (2020).

[59] A. L. Marchant, T. P. Billam, M. M. H. Yu, A. Rakonjac, J. L. Helm, J. Polo, C. Weiss, S. A. Gardiner, and S. L. Cornish, Quantum reflection of bright solitary matter waves from a narrow attractive potential, Phys. Rev. A **93**, 021604 (2016).

[60] E. M. Seroka, A. V. Curiel, D. Trypogeorgos, N. Lundblad, and I. B. Spielman, Repeated measurements with minimally destructive partial-transfer absorption imaging, Opt. Express **27**, 36611 (2019).

[61] C. Raman, R. Onofrio, J. M. Vogels, J. R. Abo-Shaeer, and W. Ketterle, Dissipationless Flow and Superfluidity in Gaseous Bose-Einstein Condensates, J. Low Temp. Phys. **122**, 99 (2001).

[62] H. Kiehn, V. P. Singh, and L. Mathey, Superfluidity of a laser-stirred Bose-Einstein condensate, Phys. Rev. A **105**, 043317 (2022).

[63] C. Weitenberg and J. Simonet, Tailoring quantum gases by Floquet engineering, Nat. Phys. **17**, 1342 (2021).

[64] R. A. Hart, P. M. Duarte, T.-L. Yang, X. Liu, T. Paiva, E. Khatami, R. T. Scalettar, N. Trivedi, D. A. Huse, and R. G. Hulet, Observation of antiferromagnetic correlations in the Hubbard model with ultracold atoms, Nature (London) **519**, 211 (2015).

[65] A. J. Kollár, A. T. Papageorge, K. Baumann, M. A. Armen, and B. L. Lev, An adjustable-length cavity and Bose-Einstein condensate apparatus for multimode cavity QED, New J. Phys. **17**, 043012 (2015).

[66] K. Kroeger, N. Dogra, R. Rosa-Medina, M. Paluch, F. Ferri, T. Donner, and T. Esslinger, Continuous feedback on a quantum gas coupled to an optical cavity, New J. Phys. **22**, 033020 (2020).